LASER & PHOTONICS REVIEWS

Laser Photonics Rev. **7**, No. 1, 60–82 (2013) / **DOI** 10.1002/lpor.201100032

REVIEW ARTICLE

Abstract Whispering gallery mode (WGM) optical microresonators have attracted intense interests in the past decades. The combination of high quality factors (Q) and small mode volumes of modes in WGM resonators significantly enhances the light-matter interactions, making them excellent cavities for achieving low threshold and narrow linewidth lasers. In this Review, the progress in WGM microcavity lasers is summarized, and the laser performance considering resonator geometries and materials as well as lasing mechanisms is discussed. Label-free detection using WGM resonators has emerged as highly sensitive detection schemes. However, the resolution is mainly limited by the cavity Q factor which determines the mode linewidth. Microcavity lasers, due to their narrow laser spectral width, could greatly improve the detection resolution. Some recent developments in sensing using microcavity lasers are discussed.

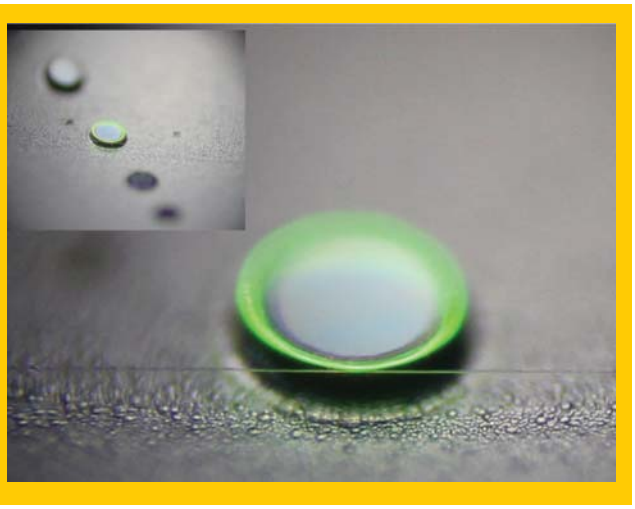

Whispering gallery microcavity lasers

Lina He, Şahin Kaya Özdemir, and Lan Yang

1. Introduction

Since the realization of the first laser in 1960 using ruby as the active material [1], many active media, i. e., materials that can generate optical gain such as semiconductors, quantum dots (QDs), organic dyes, organic polymers, and rare-earth metal ions, have been studied for their suitability for lasing. Meanwhile, a large variety of cavity configurations have been developed and implemented to decrease cavity losses and to improve light amplifications. Lasing wavelength, spectral width of the lasing line, and lasing threshold are the fundamental parameters to characterize a laser. These parameters depend on the quality factor (Q) of the laser cavity and the volume (V) of the resonant mode. While the former defines the optical loss experienced by photons in the laser cavity, the latter determines the level of light field confinement in the cavity. A large Q/V ensures strong coupling between the cavity field and the active material [2–4], implying the possibility of realizing low threshold and narrow linewidth lasers [5–7].

Whispering gallery mode (WGM) microresonators have been demonstrated as excellent candidates for constructing low threshold and narrow linewidth lasers, thanks to their low optical losses (i. e., high Q) and miniature sizes (i. e., small V). In this paper, we will review the progress of various WGM microcavity lasers and briefly introduce their applications for high-performance label-free sensing and detection. The review is organized as follows. In Sect. 2, we introduce the basic concept of WGM resonators, including their characteristics and the advantages compared to other types of laser cavities. In Sect. 3, we give a brief review on the progress of WGM microlasers in the past decades. In Sect. 4, we present some of our experimental and theoretical results on WGM microtoroidal lasers with erbium (Er^{3+}) ions as the active material. In Sect. 5, we discuss recent progress on directional laser emission. Section 6 reviews the sensing applications of WGM microlasers. Finally, Sect. 7 includes the conclusions and the outlook for future research in this exciting field.

2. WGM microresonators

Optical resonators play an important role in modern optics. A conventional optical cavity or resonator consists of two or more mirrors arranged in such a way that light bounces back and forth in a closed path for multiple times (Fig. 1). When the round trip optical path length is equal to an integer number of the light wavelength, constructive interference of light takes place inside the cavity. This is known as the resonant condition. In order to achieve a high light intensity in a cavity, one needs to decrease the cavity size allowing strong light confinement and to increase the reflectivity of the mirrors reducing optical losses. Achieving these requirements is technically challenging and expensive for mirror-based cavity constructions. However, they can be easily fulfilled

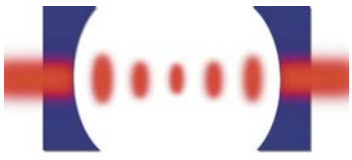

Figure 1 (online color at: www.lpr-journal.org) Schematic representation of a Fabry-Perot cavity.

Department of Electrical and Systems Engineering, Washington University, St. Louis, MO 63130, USA
Corresponding authors: e-mail: heln@ese.wustl.edu, ozdemir@ese.wustl.edu, yang@ese.wustl.edu

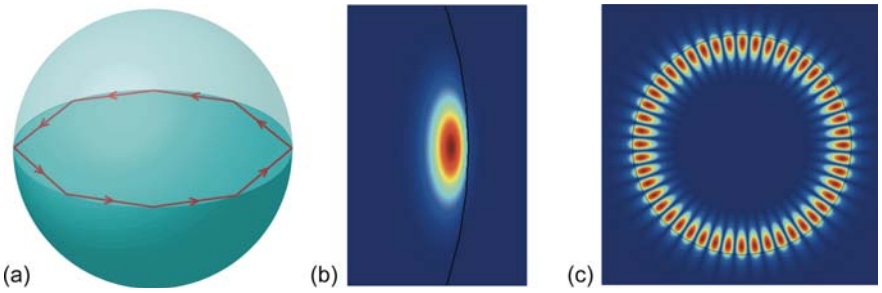

Figure 2 (online color at: www.lpr-journal.org) (a) A ray-optics description of light propagation in a microsphere resonator. (b) Cross-sectional mode distribution of a fundamental WGM along the radial and polar directions. (c) Mode distribution in the equatorial plane of the microsphere resonator.

by a particular class of monolithic resonators with circular shapes, referred to as WGM resonators [8–15]. In these resonators, light propagates along the resonator-surrounding interface via total internal reflection with the guided modes known as whispering gallery modes. Resonant condition in WGM resonators is approximated as $2\pi nR = m\lambda$, where n is the effective refractive index of the resonator, R is the resonator radius, m is an integer giving the number of wavelengths in a round trip of the cavity, and λ is the light wavelength.

Figure 2 shows the ray-optics picture of light propagation in a microsphere resonator and the electrical field distributions of a fundamental mode near the surface and along the equatorial plane of the microsphere. Light field trapped inside the resonator has an exponentially decaying evanescent tail extending into the surrounding medium with the decay length of a few hundred nanometers. Evanescent coupling of light in and out of WGM resonators has been realized using various methods such as prism [16], waveguide [17], half block [18, 19], angle-polished fiber tip [20], and tapered fiber [21]. Among these methods, strip waveguide and fiber taper coupling schemes have emerged as the choices in many applications. Fiber tapers have been generally accepted as ideal coupling schemes, and a coupling efficiency above 99% has been reported [22, 23].

The unique combination of high quality factor and tight mode confinement in a WGM microcavity significantly enhances the light field, leading to an extraordinarily high light intensity inside the cavity with a modest input power, which enables strong interactions between the light field and the objects placed in the cavity mode volume. For a microlaser configuration, such strong interactions could enhance the pumping efficiency, thereby reducing the lasing threshold. Power enhancement η in a WGM resonator can be expressed as [11]

$$\eta = \frac{P_c}{P_{\text{in}}} = \frac{1}{\tau_r} \frac{4\kappa_{\text{ex}}}{4\Delta\omega^2 + (\kappa_0 + \kappa_{\text{ex}})^2} \tag{1}$$

where P_{in} and P_c denote the input power and the intracavity circulating power, respectively, τ_r is the photon round trip time, $\Delta\omega$ represents the detuning between the input light frequency and the resonant mode frequency ω_c, $\kappa_0 = \omega_c/Q_0$ is the intrinsic cavity loss and $\kappa_{\text{ex}} = \omega_c/Q_{\text{ex}}$ represents the coupling loss with Q_0 and Q_{ex} being the intrinsic and coupling quality factors. When the incident light frequency is on resonance with a WGM in the cavity ($\Delta\omega = 0$), at critical coupling point ($\kappa_0 = \kappa_{\text{ex}}$), the power enhancement is maximized and yields

$$\eta = \frac{P_c}{P_{\text{in}}} = \frac{Q_0}{\tau_r \omega_c} . \tag{2}$$

For example, for a silica (SiO_2) microsphere of $R = 15\,\mu\text{m}$, $n = 1.45$, and $Q_0 = 10^8$, at resonant wavelength $\lambda_c = 1550\,\text{nm}$, the corresponding photon lifetime is $\tau_l = Q_0/\omega_c = 82\,\text{ns}$ and the volume of the fundamental WGM is $283\,\mu\text{m}^3$. An input power of $P_{\text{in}} = 1\,\text{mW}$ coupled into the cavity will build up a circulating power as high as $P_c \sim 180\,\text{W}$ corresponding to a power enhancement of $\eta \sim 1.8 \times 10^5$. The circulating power is concentrated in an effective mode area of $3\,\mu\text{m}^2$ leading to a high light intensity of $6\,\text{GW/cm}^2$. Therefore, WGM resonators are especially suitable as laser cavities for ultra-low threshold lasing.

3. WGM microlasers

Developments in fabrication technologies have made it possible to fabricate microscale WGM resonators with a variety of materials and shapes. Resonators made from different liquid and solid materials such as water droplet, silica, semiconductor, polymer, etc., have been reported. Various geometries, including microspheres, disks, rings, toroids, cylinders, and bottles, have been demonstrated and used in applications ranging from sensing to microcavity lasers [12–15]. Lasing in WGM resonators can be achieved by either introducing active materials to the resonator or using intrinsic nonlinearities of the resonator material. Combination of high Q resonators and different gain materials, e. g., organic dyes, QDs, and rare-earth ions, leads to a variety of laser configurations covering a wide lasing spectral range from ultraviolet to infrared. In this section we briefly introduce some of the pioneering works on microlasers in various forms of materials and discuss the present status of the field.

3.1. Liquid droplet

The idea of using liquid droplets as optical resonators was first introduced in 1977 by Ashkin and Dziedzic [24]. Liquid droplet resonators are formed by strong surface tension in liquid systems, which results in very smooth boundaries. Light is confined along the droplet surface and propagates through total internal reflection at the liquid-air interface. In liquid carbon disulfide (CS_2) microdroplets, Q factors

on the order of 10^8 were reported, with Rayleigh scattering losses being the main limiting factor [25]. Quality factors exceeding 10^9 in the ultraviolet region were demonstrated in liquid hydrogen droplets [26].

Laser emission in liquid droplets was first observed in Rhodamine 6G (R6G) doped ethanol droplets with diameter of 60 μm pumped by a continuous-wave (CW) argon laser [27]. The threshold pump intensity was approximately 35 W/cm^2. Laser emission was also observed in ethanol droplets containing Rhodamine 590 and Rhodamine 640 [28]. The lasing spectral behavior of R6G doped water microdroplets was studied in [29]. Schäfer et al. [30] reported lasing from water-glycerine microdoplets containing CdSe/ZnS nanocrystal QDs (Fig. 3a). Single-mode lasing was observed for cavity diameters less than 10 μm with a pump threshold of 53 mJ/cm^2. Multimode operation was reported for larger droplets with sizes up to 41 μm. The Q factor of the liquid microsphere was measured as 6.5×10^3. This low Q factor was attributed to pump pulses induced shape distortions which increased the losses. In a recent work, Humar and Muševič [31] demonstrated lasing in dye doped nematic liquid-crystal (LC) droplets floating in water. Low lasing threshold of 0.25 mJ/cm^2 was observed for a 13.7 μm droplet.

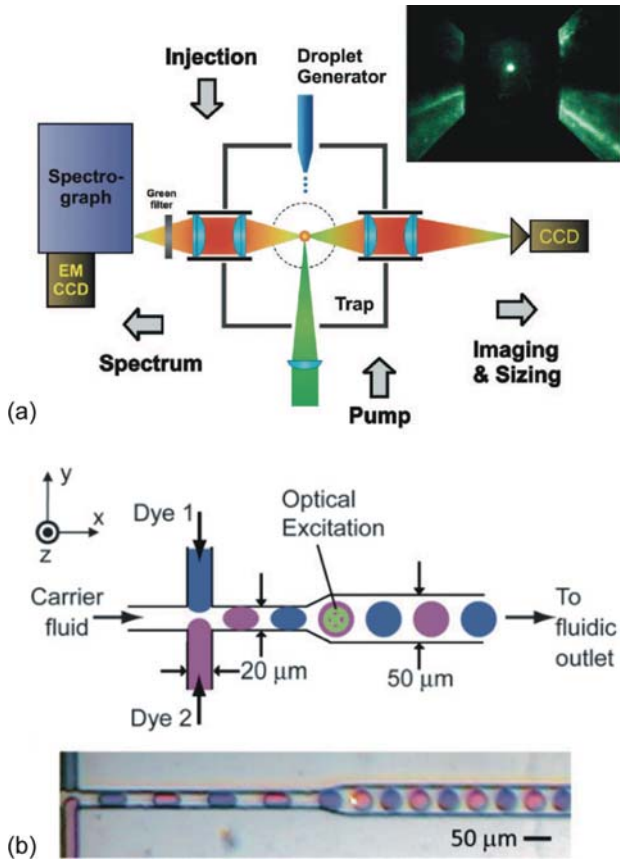

Figure 3 (online color at: www.lpr-journal.org) Liquid droplet lasers. (a) Schematic diagram showing the experimental setup to measure the lasing from a liquid droplet in air. An electrodynamic endcap trap is used to levitate a microdrop. The droplets are injected vertically from above the trap and the pump beam is incident vertically from below. The scattered light is collected on either side of the trap for imaging and spectral analysis. Inset: Picture of trapped microdrop. (Reprinted with permission from [30]. Copyright 2008 American Chemical Society.) (b) Schematic diagram (upper) and optical micrograph (lower) of a two-color droplet laser. It consists of two opposing T-junctions allowing generation of droplets containing two different dyes: rhodamine 560 (pink) and oxazine 720 (purple). (Reprinted with permission from [36])

In the aforementioned work, the liquid droplets were either arrayed in a falling vertical line, or suspended in air or water by techniques such as optical levitation and electrodynamic trap. It is challenging to control the droplet positions in those schemes. Recent studies showed that this problem can be solved by placing liquid droplets on a superhydrophobic solid substrate surface. This would stabilize the positions of the droplets without significantly disturbing their shapes [32]. Lasing from such droplets doped with Rhodamine B has been demonstrated with a threshold of 750 J/cm^2 [33].

Recently, liquid droplets have been incorporated into microfluidic systems for a wide range of applications [34]. Lasing from dye doped droplets in a microchannel was demonstrated in [35, 36]. In a microfluidic system, a T-junction can be used to generate droplets. When the carrier liquid and the dye solution meet at the T-junction, a series of dye droplets separated by the carrier liquid is formed due to the shear forces. The sizes of the droplets can be adjusted by controlling the fluid flow rates, the channel widths, and the relative viscosity of the two liquids [34]. Tang et al. [36] described a two-color dye laser based on a train of alternating droplets containing two different dyes generated by two T-junctions (Fig. 3b). This system was capable of switching the lasing wavelength between 580 nm and 680 nm at a frequency up to 3.6 kHz.

Although liquid droplet lasers allow large size tunability and doping flexibility, experiments with droplets suffer from the difficulties in manipulation, short lifetime due to the evaporation of droplet, mechanical instabilities, and low light coupling efficiency. Recently, a quasi-droplet ring resonator laser based on a fused silica micro-bubble with an extremely thin wall was reported [37]. It mimics the droplet resonator in air and is capable for easy manipulation and light coupling. Laser emission was achieved using R6G in methanol with a threshold of 300 nJ/mm^2.

3.2. Glass

The first reported ultra-high Q microscale solid WGM resonators were microspheres with diameters of 40–400 μm fabricated from fused quartz with measured Q factors above 10^8 [9]. Initial results with glass spheres indicated that Q values in excess of 10^9 were possible [10]. Gain materials can be incorporated into a solid resonator by various approaches, such as directly fabricating the resonator from an active medium doped material [38–40], coating the resonator with light emitters [41–46], and doping the resonator with gain materials by ion implantation [47]. In [38], laser

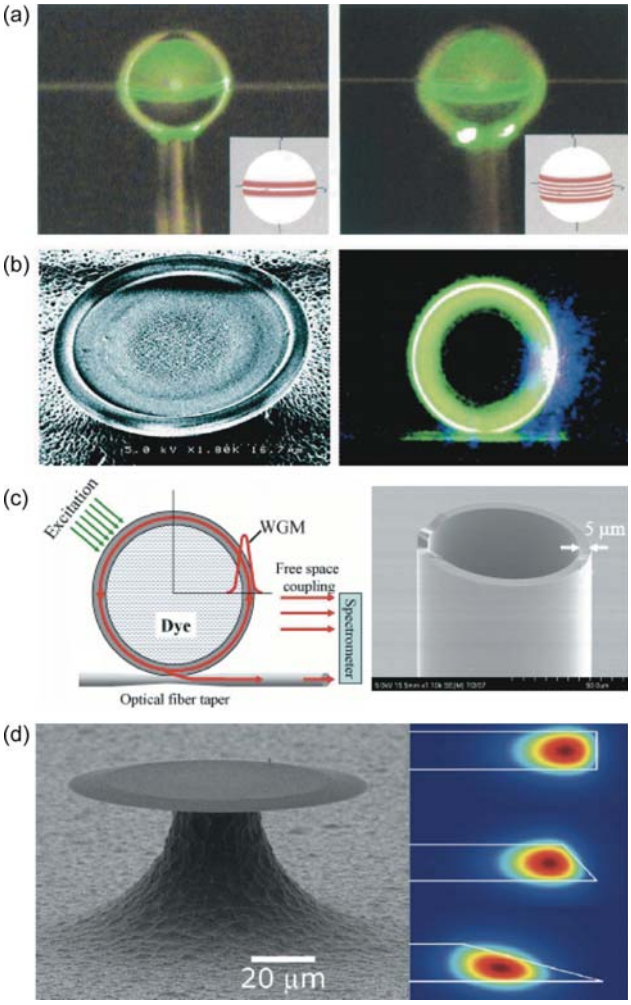

Figure 4 (online color at: www.lpr-journal.org) Glass microcavity lasers. (a) Lateral emission distributions of different WGMs in a fiber taper coupled microsphere. The green rings are upconverted photoluminescence. The inset shows spherical harmonics. (Reprinted with permission from [41]) (b) Scanning electron micrograph (SEM) of a QDs coated toroidal microcavity (left) and optical micrograph showing QDs emission from a microtoroid cavity (right). (Reprinted with permission from [56]. Copyright 2006, American Institute of Physics.) (c) Concept of OFRR dye lasers (left) and SEM image of an OFRR (right). (Reprinted with permission from [68]) (d) SEM image of a silica microdisk on a silicon wafer (left) and simulation of the intensity profile of the fundamental WGM in a microdisk for three wedge angles: 90°, 45°, and 22°. (Reprinted with permission from [71])

action was obtained from a silica microsphere formed by heat-fusing the tip of a neodymium (Nd^{3+}) doped silica wire. For a cold-cavity (i. e., active medium is not excited) Q factor of 2×10^8, the absorbed pump power at lasing threshold was measured as low as 200 nW for resonant pumping. Yang and Vahala [41] coated silica microspheres with Er^{3+}-doped silica sol-gel films to obtain single-line laser emission in 1550 nm band (Fig. 4a). They reported a lasing threshold of 28 μW and single-mode laser output powers up to 10 μW. Sol-gel process is widely used to prepare bulk materials or thin films based on hydrolysis and condensation reactions of specific precursors, such as metal alkoxides [48]. It allows precise control of the dopant concentration which strongly affects the laser dynamics. Lin et al. [44] demonstrated single-mode lasing at 1088.2 nm with threshold as low as 65 nW and slope efficiency about 7% in silica microspheres functionalized by Nd^{3+}-doped gadolinium oxide nanocrystals. Shopova et al. [45] reported laser emission in the range 1240–1780 nm from HgTe QDs coated silica microspheres of diameter 950 μm with threshold pump powers less than 2 μW at 830 nm.

On-chip silica microtoroidal resonators provide high Q factors ($\sim 4 \times 10^8$), owing to the minimized scattering losses from the smooth resonator surface created by surface tension during a laser reflow process [49]. In the toroidal-shaped structure, light is confined in both radial and polar directions, ensuring smaller mode volumes and fewer resonant modes than those in microspheres of the same size [50]. This allows single-mode lasing over a large range of pump powers. Laser action was reported in rare-earth ion and QD (Fig. 4b) doped silica microtoroids with lasing threshold varying from a few microwatts to hundreds of microwatts depending on the cold-cavity Q factor, dopant concentration, and microtoroid size [51–56]. To reduce the threshold pump power, resonant pumping is usually used to efficiently excite the active medium. This requires a laser as the pumping source whose frequency matches the resonant condition of the laser cavity. To avoid this requirement, Rotschild et al. [57] demonstrated a microlaser with a direct-illumination, non-resonant pump. This was done by cascaded energy transfer in three organic dyes coated on a microcavity. The emission band of one dye matched the absorption peak of a different dye material, significantly increasing the efficiency of broad band pumping.

Light emission from solid-state microlasers in water was first obtained by Ostby et al. [58] from ytterbium (Yb^{3+}) doped silica microtoroids. The small absorption of water in Yb^{3+} emission band (i. e., 1040 nm) reduces cavity losses making it possible to generate laser emission in water. The demonstrated microlaser in water had threshold of 14 μW and slope efficiency of 0.5% when the maximum output laser power was 2 μW. Laser emission in aqueous environment holds the potential for using microlasers as high-performance biosensing platforms [59].

Another class of widely used WGM cavities is cylindrical microresonators, which employ micro-sized glass capillaries with wall thickness of tens to hundreds of microns [60]. In these resonators, light propagates along the circular cross section of the capillary. Such structures naturally integrate WGM ring resonators with microfluidic channels, providing a promising platform for applications in biochemical sensing and lasing. Lasing from dyes and QDs in various configurations of cylindrical microcavities has been studied [61–69]. Different lasing wavelengths are achieved by simply changing the dyes or QDs solution flowing through the capillary.

Knight et al. [61] observed laser emission from R6G doped quinoline flowing in a silica capillary fiber. Due to the higher refractive index of the dye solvent (1.626) than

that of the silica capillary (1.458), WGMs could only exist around the inner capillary-liquid boundary making it difficult to couple the laser light out of the cavity. The pump threshold for laser emission was approximately 0.1 kW/cm^2. The gain medium can also be placed in the evanescent field region of WGMs to achieve lasing [62–64]. Moon et al. [62] reported a microcavity laser composed of a cylindrical microcavity surrounded by R6G dye molecules in an ethanol solution. Laser emission was observed at about 600 nm with cavity Q of 3×10^7. In [64], linearly polarized emission of quantum rods was demonstrated in a cylindrical microcavity comprising an optical fiber within a glass capillary tube. In this cavity configuration, the WGMs were confined in the fiber due to its higher refractive index than that of the surrounding quantum rods solution. Lasing was generated due to the gain in the evanescent field of WGMs near the fiber surface. In addition to WGMs, waveguide mode was also reported in cylindrical shell resonators for laser emission [65]. In [67, 68], laser oscillation was demonstrated in an opto-fluidic ring resonator (OFRR) filled with R6G dye doped solvent (e. g., ethanol, chloroform, and quinoline). The OFRR was obtained by stretching a fused silica capillary under heat to obtain a wall thickness of a few microns which was thin enough for the high Q WGMs extending into the core to interact evanescently with the gain medium in it. The thin wall also enabled outcoupling of the laser emission through a tapered fiber that was in touch with the OFRR. The lasing mechanism is shown in Fig. 4c. Due to the high Q factor of the WGM residing mostly inside the silica capillary, a low threshold of 25 nJ/mm^2 was achieved.

Microdisks have been used to achieve lasing in WGM microcavities made of glass. Liu et al. [70] fabricated ultraviolet silica microdisk lasers on a silicon substrate. A thin layer of zinc oxide (ZnO) serving as the gain medium was deposited on the top of a silica microdisk. The hybrid ZnO/SiO_2 microdisk was optically pumped at wavelength 355 nm, while the laser emission was at ~390 nm. The lasing threshold pump energy was 0.85 nJ/pulse at a pump pulse duration of 20 ps and repetition rate of 10 Hz. Kippenberg et al. [71] doped silica microdisks with Er^{3+} ions through ion implantation which could precisely control the ion distribution in the disk yielding overlap of the Er^{3+} ions with the WGMs (Fig. 4d). The Q factor of the doped microdisk was observed as 1.5×10^6 at 1428 nm and gradually reduced to 2×10^5 at 1470 nm due to light absorption by Er^{3+} ions. Laser emission was obtained in 1550 nm band at a pump threshold of 43 μW.

3.3. Semiconductor

Semiconductor WGM resonators support strongly confined modes due to the large refractive index contrast between the resonator material and its surrounding. The resonator diameter could be shrunk down to a few microns. Lasing from semiconductor microdisk cavities with a variety of active materials has been reported [72–80].

McCall et al. [72] reported a microlaser based on an InP/InGaAsP microdisk with optically pumped InGaAs quantum wells on top of the disk. When cooled with liquid nitrogen, single-mode lasing at 1.3 μm and 1.5 μm was observed with pump threshold below 100 μW. Cao et al. [74] achieved lasing in InAs QDs embedded GaAs microdisks. For a 3 μm microdisk at 77 K, lasing in the range of 945–1005 nm with threshold around 20 μW was observed when the QDs were pumped with a CW HeNe laser at 633 nm. Baba and Sano [76] reported CW lasing at 1.55 μm in a photopumped GaInAsP microdisk laser at room temperature. The minimum threshold pump power was 19 μW for a 1.4-μm diameter disk.

Low temperature (10 K) lasing in a GaN/InGaN microdisk was previously observed under pulsed optical pumping [78]. The Q factor of the microdisk was on the order of 4600 and the lasing threshold was 12.1 W/cm^2. The first CW lasing in a GaN microdisk at room temperature was reported in [79]. A threshold of 300 W/cm^2 for lasing at 428 nm was observed from a 1.2-μm microdisk.

In [80], electrically pumped CW lasing in a 7.5-μm diameter InP microdisk on a silicon platform was described. In the laser structure, the microdisk was etched in a thin InP-based layer bonded on top of a silicon-on-insulator (SOI) waveguide wafer, as shown in Fig. 5a. The threshold current was 0.5 mA, and the unidirectional slope efficiency was 30 μW/mA, with a maximum CW output power of 10 μW. Fujita et al. reported CW lasing at 1.563 μm from a GaInAsP-InP microdisk injection laser with a low threshold current of 40 μA [81, 82].

Semiconductor micropillars [83, 84] were demonstrated to support high Q WGMs with small mode volumes. Lasing from GaAs/AlAs micropillars with embedded QDs under both electrical pumping [85] and optical pumping [86] has been reported. In [85], a threshold current as low as 8 μA at 10 K was observed for a 1.5-μm micropillar with Q factors exceeding 10000 (Fig. 5b). In [86], lasing was observed for pillar diameters in 3–4 μm range at temperature range 5–100 K. Threshold pump power was 7 mW. Efficient heat sink provided by the pillar geometry led to a stable emission wavelength and a spectral narrowing above lasing threshold.

A GaInAsP/InP microgear, composed of a microdisk and a rotationally symmetric Bragg grating, was realized to generate room-temperature CW laser emission in the wavelength range of 1.60–1.67 μm with a low threshold of 17 μW [87]. The internal disk diameter was in the range of 2.2–3.2 μm, and the grating depth was 50–270 nm (Fig. 5c). The authors demonstrated that the microgear showed a higher Q factor than its counterpart microdisk due to minimization of the radiation field by the Bragg grating, and thus exhibited a lower lasing threshold.

To avoid high optical bending losses, most microdisk lasers have diameters over 1 μm. However, submicron lasers enable large scale integration and have important applications in nanophotonic circuits and highly localized chemical and biological sensing. Visible [88] and near infrared [89] single-mode lasing in semiconductor submicron disk lasers has been demonstrated for disk diameters of approximately 600 nm (Fig. 5d). Submicron disks can be fabricated either by electron-beam lithography and dry etching [88], or by photolithography and wet etching [89]. Small cavity mode

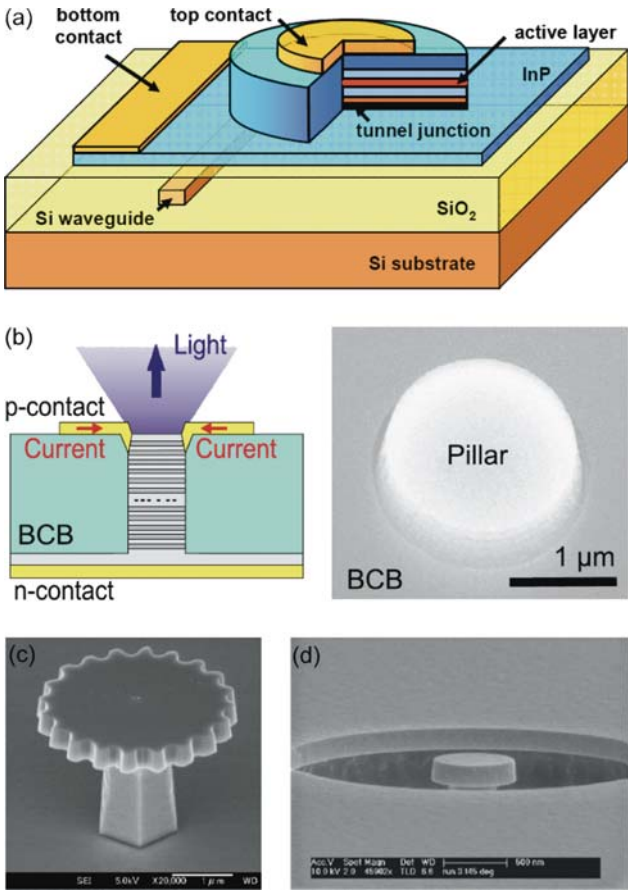

Figure 5 (online color at: www.lpr-journal.org) Semiconductor microcavity lasers. (a) Schematic drawing of a heterogeneous microdisk laser structure, showing the disk cavity, SOI wire waveguide, bottom contact layer, tunnel junction, and metal contacts. (Reprinted with permission from [80]) (b) Schematic view of an electrically pumped micropillar laser structure (left) and SEM image of a 2-μm diameter micropillar laser. (Reprinted with permission from [85]. Copyright 2008, American Institute of Physics.) (c) SEM image of a microgear laser. Microroughness of the disk surface and sidewall is less than 5 nm. (Reprinted with permission from [87]. Copyright 2002, American Institute of Physics.) (d) SEM image of a submicron disk laser with diameter of 645 nm. (Reprinted with permission from [88]. Copyright 2007, American Institute of Physics.)

volumes of $0.03\,\mu m^3$ and low lasing thresholds at around 50 μW were reported. Recently, Chen et al. [90] demonstrated the growth of single-crystal GaAs hexagonal nanopillars on silicon at 400 °C. The nanopillars consisted of InGaAs active core and GaAs shell, and had tiny footprints of $\sim 0.34\,\mu m^2$. The tapered nanopillars supported WG-like helically propagating cavity modes with measured Q factors of 319. Laser oscillation at room temperature was achieved at a threshold of $\sim 93\,\mu J/cm^2$. The lasing wavelength could be controlled by varying the indium composition during nanopillar growth.

Quantum cascade (QC) lasers are another type of powerful semiconductor laser sources that fill the increasing need for high performance mid-infrared lasers. They are promising light sources for molecular detection with applications in environmental sensing and medical diagnostics [91, 92]. QC lasers rely on modification of the electronic energy band in semiconductor materials due to quantum confinement in thin film structures. Laser emission is generated via intersubband transitions in a superlattice formed by multiple closely stacked thin film structures. The fundamental difference of QC lasers from conventional lasers is that their wavelengths can be flexibly tailored over a wide range by modifying the thickness of the materials in the active region.

The first QC laser was demonstrated in 1994 at cryogenic temperatures [93]. Following this pioneering work, lasing from QC lasers based on WGM microcavities has been reported covering mid-infrared to far-infrared wavelength range [94–99]. Faist et al. [94] reported QC microdisk lasers at wavelength of 5 μm. The Q factor of the microdisk was around 3500. Threshold currents of 2.85 mA were observed for disks of 17 μm in diameter at 15 K. Long wavelength lasing at 9.5 μm and 11.5 μm from microdisk QC lasers was reported in [95]. Microcavities for QC lasers emitting at terahertz frequencies have also been investigated [97, 98]. Audet et al. [99] fabricated mid-infrared QC lasers with spiral-shaped microresonators to obtain high power emission and single-mode operation. The lasers can operate either in pulsed mode at room temperature with peak optical power greater than 20 mW, or in CW mode at temperatures up to 125 K.

3.4. Crystalline

Optical crystals as resonator materials provide a few advantages over fused silica [100–102]. The near ideal lattice structures of crystals provide a less lossy platform than fused silica. In addition, these materials are transparent to a broad wavelength range from ultraviolet to mid-infrared. Moreover, crystals may suffer less, or not at all, absorption loss caused by chemosorption of OH^- ions and water which is a limiting factor for Q of silica resonators. Another advantage of crystalline cavities is that they enable studies of high nonlinearities in optical materials. Fabrication of crystalline WGM resonators was done by mechanical polishing techniques. Savchenkov et al. [100] demonstrated high Q resonators made of calcium fluoride (CaF_2, $Q > 2 \times 10^{10}$), sapphire (Al_2O_3, $Q > 10^9$), lithium niobate and lithium tantalate ($LiNbO_3$ and $LiTaO_3$, $Q > 2 \times 10^8$). Lasing from crystalline resonators mainly exploits optical nonlinear effects such as stimulated Raman scattering (SRS) [103], stimulated Brillouin scattering (SBS) [104], parametric oscillation [105, 106], four-wave mixing [107, 108], and harmonic generation [109, 110].

3.5. Polymer

Due to easy processing, structural flexibility, and low cost, polymer resonators are becoming increasingly competitive to devices made of other materials. They have attracted great interest in the past two decades. A variety of techniques have

been reported to fabricate polymer WGM microresonators, including molding from a master structure [111, 112], direct laser writing using two-photon absorption induced polymerization [113], direct lithographic patterning [114, 115], mechanical turning and polishing [116], and surface-tension based approach [117] (Fig. 6).

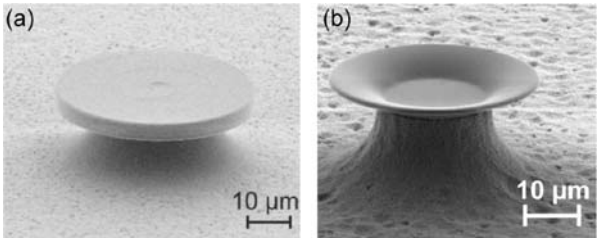

Figure 6 Polymer microcavities. (a) SEM image showing a polymeric microdisk with a diameter of 47 μm and a thickness of 4 μm fabricated via direct laser writing. (Reprinted with permission from [113]) (b) SEM image of a conical polymeric resonator obtained by electron-beam lithography and thermal heating. (Reprinted with permission from [115]. Copyright 2010, American Institute of Physics.)

Active materials can be easily doped into or coated on polymer resonators. For example, organic dyes and QDs are usually dissolved in polymer host matrix or coated on polymer resonators as gain media. Laser emission has been demonstrated in polymer microspheres [46, 118, 119], microdisks [113, 120], microrings [120], and conical microcavities [121, 122]. The microring resonator in [120] was prepared by dipping a small-diameter cylindrical silica fiber into a dye-doped polymer solution and allowing a layer of polymer to cure around the glass core by surface tension and adhesion. For a 17-μm diameter microring, the lasing threshold was near 6 mW. In [121], R6G molecules in ethanol were mixed into PMMA, from which conical cavities were fabricated by photolithography and thermal heating. Quality factors above 2×10^6 were reported for the undoped cavities. Lasing emission at around 600 nm for different dye concentrations was studied. For a pump pulse duration of 15 ns and repetition rate of 5 Hz, lasing thresholds as low as 3 nJ/pulse and narrow laser linewidths of 50 pm were observed.

Semiconducting polymer is an interesting class of polymers because of its light emission property. Examples of polymers within this class include poly(para-phenylene vinylene) (PPV) and poly(para-phenylene) (PPP). The large optical gain makes such polymers promising candidates as active materials. They can be pumped optically or electrically [123–126]. Lasing from polystyrene films containing semiconducting polymer and titanium dioxide nanocrystals in solid state was first demonstrated by Hide et al. in 1996 [127]. Conjugated polymer can either be used to fabricate WGM microcavities directly [128–130], or be coated on microcavity structures as the active medium [130–134]. In [129], laser emission from π-conjugated polymer poly(dioctyloxy) phenyl vinylene (DOO-PPV) microdisks was demonstrated. The polymer powder was dissolved in toluene and spun onto a glass substrate to form a uniform film with thickness of ~2 μm. Microdisk lasers were then fabricated from the polymer film. Tulek et al. [133] reported laser emission from a toroidal microcavity coated with DOO-PPV. Laser emission at 635 nm with a threshold of 200 pJ/pulse was obtained when the cavity was pumped by femtosecond pulses of 130 fs and repetition rate of 1 kHz at 521.6 nm.

3.6. Lasing based on nonlinear effects in WGM resonators

In addition to laser emission from active materials doped in a microresonator or coated on the resonator surface, some nonlinear effects such as SRS, SBS, and harmonic generation can generate laser emission in a wide spectral range. One advantage of nonlinear effect based lasing is its broad gain bandwidth, which widely extends the light emission band. Due to the enormous circulating light intensity build-up within a high Q WGM resonator, threshold of nonlinear processes is greatly reduced. Thus, nonlinear effect based lasing can be obtained even in resonators made of materials with small nonlinearities.

In 1985, Snow et al. [135] reported the first observation of SRS from individual droplets made of water, heavy water, and ethanol in the radius size range 20–40 μm with an input intensity threshold $\ll 10^9$ W/cm^2. Raman lasing was also reported in CCl_4 [136] and CS_2 [25] droplets. Raman lasing near 630 nm and 650 nm from glycerol-water [137] and pure water [138] microdroplets on a superhydrophobic surface was described. In [138], the Q factors of WGMs exhibiting Raman lasing were $\sim 5 \times 10^6$. Zhang and Chang [139] observed SBS generation from water and methanol microdroplets. Raman laser in silica microspheres was reported in [140] with threshold pump power of 86 μW. Silica microtoroid Raman laser was demonstrated with threshold less than 100 μW and conversion efficiency greater than 45% [141, 142]. In [142], fundamental Raman laser linewidth as low as 3 Hz with a maximum unidirectional output power of 223 μW was obtained. Lasing based on SRS and SBS has been observed in CaF_2 microcavities with lasing thresholds of 15 μW and 3 μW, respectively [103, 104]. Raman lasing in silicon was first demonstrated in a rib waveguide with specially designed coatings to form a Fabry-Perot resonator [143, 144]. Two-photon absorption in silicon, which induced nonlinear optical loss, was reduced by introducing a reverse biased p-i-n diode embedded in the silicon waveguide. Later in [145], Rong et al. reported a silicon Raman laser based on a ring cavity structure with lasing threshold of 20 mW and slope efficiency of 28% (Fig. 7a). The laser spectral linewidth was less than 100 kHz.

Third harmonic (TH) generation in WGM resonators was first observed in a CCl_4 droplet when pumped with a pulse laser at intensity ~ 0.5 GW/cm^2 [146]. Carmon and Vahala [147] demonstrated visible continuous emission from a silica microtoroid via TH generation with pump powers less than 300 μW. The emission was verified to scale cubically with the pump power. In [102, 109, 110], generations of second, third, and forth harmonic modes were

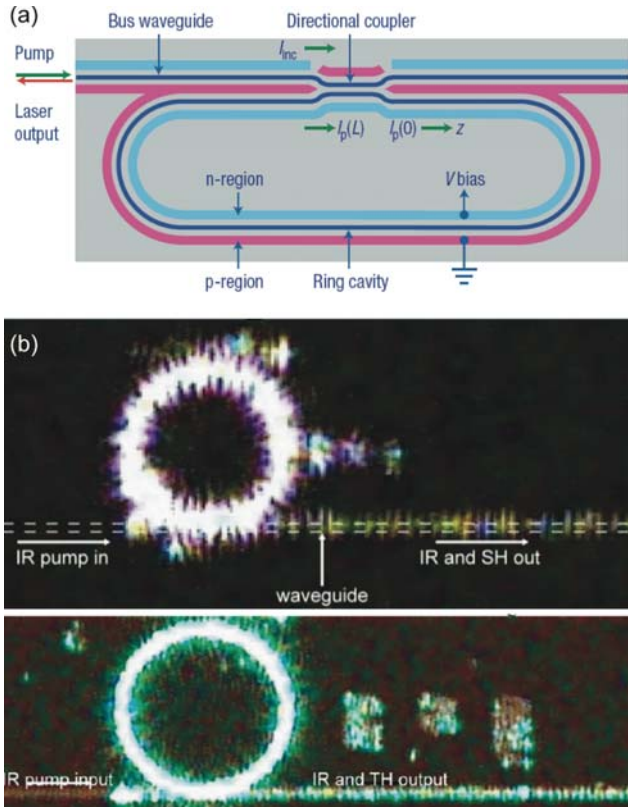

Figure 7 (online color at: www.lpr-journal.org) Microcavity lasers based on nonlinear effects. (a) Schematic layout of a silicon ring laser cavity with a p-i-n structure along the waveguides. (Reprinted with permission from [145]) (b) Top view visible CCD camera images of a microring resonator generating SH (upper) and TH (lower) light from an infrared pump. (Reprinted with permission from [150])

observed in periodically poled $LiNbO_3$ disk resonators, thanks to the high Q factors and the quasi-phase matching. Fürst et al. [148] presented the first natural phase matching for 1064 to 532 nm optical frequency doubling in a high Q ($> 10^7$) WGM resonator made of MgO-doped $LiNbO_3$. Phase matching was achieved relying on the fact that the pump and signal modes in the crystal resonator exhibited different responses to the resonator temperature or to the bias voltage applied to the resonator. This allowed continuous tuning of the relative frequency between the pump and signal modes until phase matching was satisfied [149]. Recent work in [150] reported second harmonic (SH) and TH generation in silicon nitride ring resonators. When the ring resonator was pumped at a resonance near 1554 nm for an input pump power of 3 mW, SH was generated at 777.1 nm. The TH generation at 520.1 nm was observed by pumping at a resonance near 1560 nm (Fig. 7b).

Cascaded nonlinear process can extend the wavelength range of existing laser sources and broaden the adopted pump wavelengths. In such a process, one lasing output acts as the pump for the second gain mechanism. Efficient cascaded operation is made possible by the ultra-high Q factors of WGM resonators. Cascaded Raman laser has been demonstrated in different resonators. For example, in a CCl_4 droplet of radius 35 μm, cascaded Raman generation as high as the fourteenth order was observed [28]. The first observation of cascaded Raman lasing in silica microspheres was reported in [151]. With pump power less than 900 μW near 980 nm, the fifth-order Raman lasing was achieved. Grudinin and Maleki [103] reported Stokes components up to the eighth order in a CaF_2 resonator at a pump power of 1 mW. Second-order, CW Raman lasing at 1848 nm was achieved in a silicon ring resonator using a 1550 nm pump source at a threshold power of 120 mW [152]. The maximum output power exceeded 5 mW. Figure 8 presents our measurement results of second-order Raman lasing from a silica microtoroid with diameter of 40 μm and Q factor of 10^8.

4. Lasing from Er^{3+}-doped WGM resonators

Among different gain materials, rare-earth ions (e. g., Er^{3+}, Yb^{3+}, Nd^{3+}, etc) are popular dopants for solid-state lasers due to their high efficiency, long upper-level lifetime, ability to generate short pulses, and wide emission spectrum spans from 0.3 to 3 μm [155]. In this section, we will take the Er^{3+}-doped microtoroidal resonator as an example to investigate the performance of WGM lasers.

Lasing in Er^{3+} was first demonstrated in 1965 in pulsed regime [156]. It has attracted much interest since then due to the emission at telecommunication band. Figure 9 represents the simplified energy levels of Er^{3+} ions in silica glass [157, 158]. To obtain lasing in 1550 nm wavelength band, Er^{3+} ions can be pumped in either 980 nm or 1480 nm band. When a 980 nm pump laser is used, ions are excited from ground level $^4I_{15/2}$ to excited level $^4I_{11/2}$ where they experience non-radiative decay to $^4I_{13/2}$ metastable level, and then transit back to $^4I_{15/2}$ generating photons near 1530 nm. When pumped in 1480 nm band, ions are excited from $^4I_{15/2}$ to $^4I_{13/2}$ where they experience non-radiative intersubband transitions, and finally transit radiatively to $^4I_{15/2}$ level releasing photons in 1530 nm band. Population inversion between the first excited state $^4I_{13/2}$ and the ground state $^4I_{15/2}$ can be achieved at a relatively low pump power, since the lifetime of state $^4I_{13/2}$ is long, usually on the order of millisecond.

4.1. Sol-gel fabrication of silica microtoroids

As discussed in Sect. 3, various methods have been used to introduce active media into resonators. Among them, sol-gel synthesis provides a convenient way to tailor the dopants. In this section, we will describe the preparation of Er^{3+}-doped toroidal resonators from sol-gel silica films, characterize the lasing performance, investigate the dependence of lasing threshold on various resonator parameters, and introduce the upconversion transition.

Sol-gel method is a low-cost, fast, and flexible wet-chemical synthesis technique for preparation of glasses and ceramics. The sol-gel process is based on hydrolysis

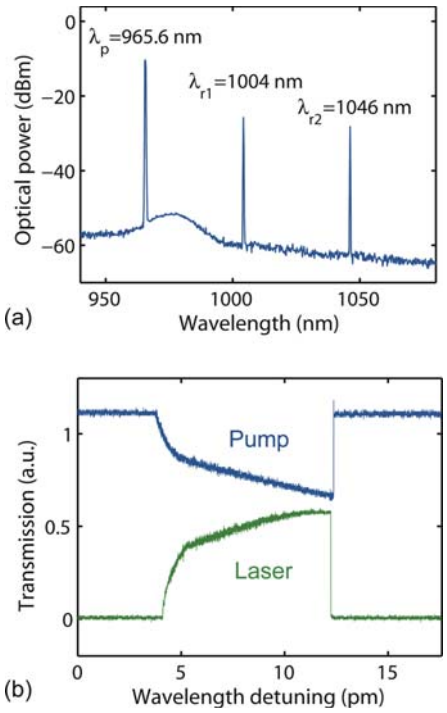

Figure 8 (online color at: www.lpr-journal.org) Cascaded Raman lasing from a silica microtoroidal resonator. (a) Laser emission spectrum obtained from an optical spectrum analyzer (OSA) showing pumping at 965.6 nm, and the first and second order Raman lasing at 1004 nm and 1046 nm, respectively. (b) Transmission of pump (blue curve) and laser (green curve) light as the pump wavelength is finely scanned in the vicinity of the resonant mode at 965.6 nm. The pump and laser beams coupled out of the resonator are separated by a 980/1040 nm wavelength division multiplexer (WDM) and detected by two photodetectors (PDs). When the pump light is on resonance, light is coupled into and circulating in the resonator forming a resonant dip in the transmission spectrum. The high pump light intensity inside the resonator gives rise to a large gain in the Raman emission band. As the Raman gain exceeds the cavity losses, Raman laser is generated. The broad pump mode is attributed to the resonant wavelength shift caused by thermal effect due to light absorption in silica [153, 154]. The green curve in (b) characterizes the increase in the power of the lasing light, shown as two peaks above 1000 nm in (a), with the increasing pump power coupled into the resonator. Specifically, changes in the slopes of the pump and laser spectra are due to the excitation of multiple orders of Raman lasing as pump power coupling into the resonator increases to a certain level indicated by the reducing pump transmission [151].

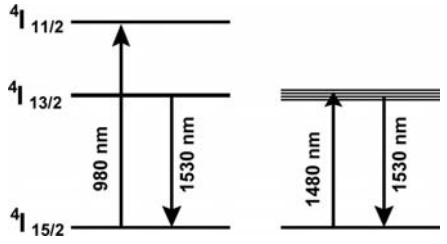

Figure 9 Simplified energy levels of Er^{3+} in silica glass for optical pumping in 980 nm and 1480 nm wavelength bands.

and condensation reactions of metal-alkoxide precursors in aqueous solution, alcohol, or other medium [48, 159]. The reaction is performed under either acid or base catalyzed condition to obtain dense films. We use sol-gel process under acid catalyzed condition to prepare silica thin films on silicon substrates from which silica toroidal resonators are fabricated. The process for synthesis of silica films can be divided into three steps: 1) Hydrolysis, Si-alkoxide is hydrolyzed by water molecules to produce a colloidal suspension (sol); 2) Condensation, hydrolyzed molecules produce Si-O-Si linkages or networks (gel); 3) Annealing, the silica-gel film is treated at high temperature to form dense glass. Dopants can be introduced into sol-gel materials by mixing relevant soluble chemicals in the precursor solutions. For example, in our experiments erbium nitrate ($Er(NO_3)_3$) is used to introduce Er^{3+} ions. The advantages of doping active medium via sol-gel technique include controllable dopant concentration, wide choice of material matrices, and flexibility and ease of adding multiple dopants.

Figure 10 is a flow chart showing the preparation of silica sol-gel film and the subsequent fabrication process of silica microtoroids. First, the sol-gel precursor solution is prepared in a Teflon beaker by mixing tetraethoxysilane (TEOS) in isopropanol alcohol (IPA) and water (H_2O) with hydrochloric acid (HCl) as catalyst. The weight ratio of IPA, H_2O, TEOS, and HCl is 6.5:0.7:0.6:6.1. Rare-earth compound (e. g., $Er(NO_3)_3$) of specific amount is mixed to the solution for desired dopant concentration. Subsequently, the solution is stirred with a magnetic bar at 500 rpm for 3 hours at 70 °C. Hydrolysis and condensation take place during this process. Afterwards, the solution is aged at room temperature for 24 hours. The aged solution is then spin-coated on a silicon wafer at 3000 rpm for 30 seconds to form a uniform layer. The coated film is heat treated in a tube furnace at 1000 °C for 3 hours to remove the residual solvent, transferring porous silica to dense glass. Then the wafer is cooled down to room temperature naturally. Finally, a uniform and smooth silica film is obtained on the silicon substrate. The film thickness after annealing depends on the

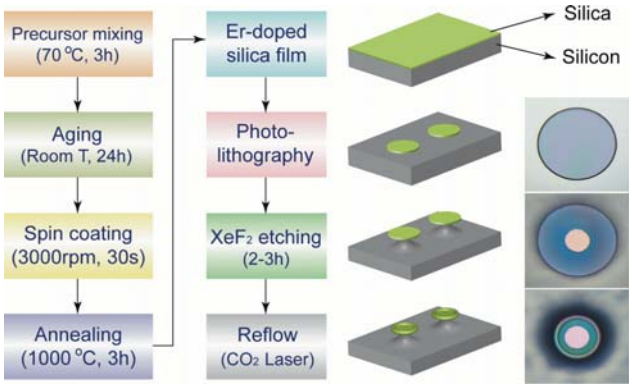

Figure 10 (online color at: www.lpr-journal.org) Fabrication flow of Er^{3+}-doped microtoroids through sol-gel process and photolithography technique. The two columns on the right show the illustrations and optical micrographs of a microdisk, under-cut microdisk, and microtoroid.

dopant concentration and the spin-coating condition. In our experiments, the thickness of one coating layer varies in the range 350–500 nm. Desired film thickness can be achieved by applying multiple coating layers. The concentration of Er^{3+} ions in the silica film is tailored by controlling the amount of $Er(NO_3)_3$ in the sol-gel precursor solution [52].

Active microtoroids are fabricated from Er^{3+}-doped silica films through a standard process of photolithography, XeF_2 etching, and CO_2 laser reflow [49, 52]. The resulting patterns after each step are shown in Fig. 10. We tested the Q factors of the microtoroids with Er^{3+} concentrations in the range of 10^{18}–2×10^{19} cm^{-3} in 1460 nm wavelength band. At each Er^{3+} concentration, multiple measurements were performed on a few microtoroids and the highest measured Q factor is plotted in Fig. 11. As Er^{3+} concentration increases, the total cavity losses increase due to light absorption by Er^{3+} ions, leading to a reduced Q factor.

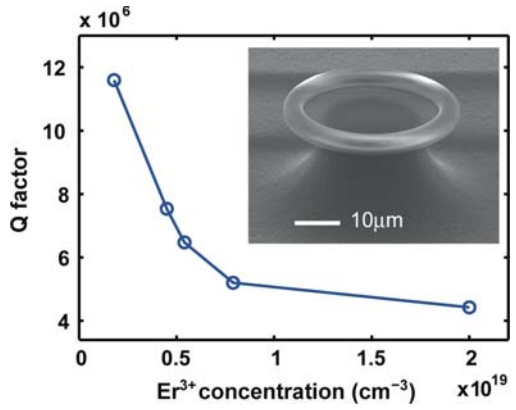

Figure 11 (online color at: www.lpr-journal.org) Measured Q factors of Er^{3+}-doped microtoroids for different dopant concentrations. Inset: SEM image of an Er^{3+}-doped microtoroid.

4.2. Characteristics of Er^{3+}-laser in 1550 nm band

The experimental setup used to characterize the microlasers is shown in Fig. 12. A CW light source in 1460 nm or 980 nm band is used to pump the cavity. A tapered fiber is used to couple light into and out of the resonator, with the coupling efficiency tuned by adjusting the gap between the taper and the resonator. A polarization controller (PC) is used to adjust the polarization state of the pump beam to optimize the coupling efficiency. The light coupled out of the resonator is sent to a WDM to separate the laser emission in 1550 nm band from the unabsorbed pump light. The outputs of the WDM are sent to an oscilloscope to observe the temporal dynamics of the lasing operation. The signals from the oscilloscope are continuously acquired by a computer. An OSA is used to record the lasing spectrum. Within the resonator, laser emission takes place and propagates along both forward and backward directions (i. e., a WGM resonator supports two counter-propagating modes at the same frequency. Here, forward denotes the clockwise and backward denotes the counter-clockwise propagating light). Laser emission is coupled out from both ends of the tapered fiber. For simplicity, we measure the lasing output transmitted in the forward direction.

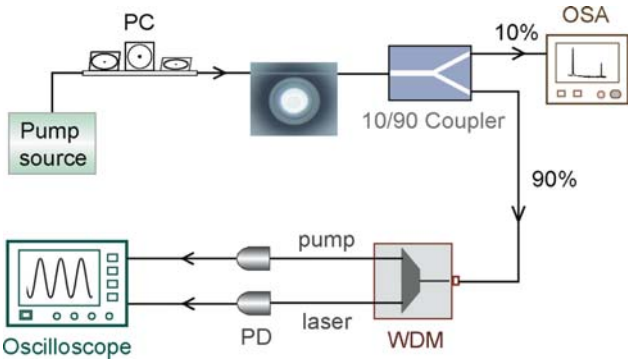

Figure 12 (online color at: www.lpr-journal.org) Schematic diagram of the experimental setup for characterizing Er^{3+}-doped microtoroids. PC: polarization controller.

In the experiments, the wavelength of the pump laser is tuned on resonance with a high Q cavity mode to achieve resonant pumping. Near the resonant wavelength, small input pump power is significantly enhanced inside the cavity to efficiently excite the Er^{3+} ions. Resonant pumping is an efficient way to greatly reduce the threshold pump power, however, it requires a tunable laser source. Alternatively, lasing can be obtained with non-resonant pumping using a high power light source, the spectrum of which overlaps with the absorption band of Er^{3+} ions. This eliminates the need for tunable pump lasers. Figure 13 shows the lasing spectrum and the laser power output as a function of the pump for an Er^{3+}-doped microtoroid. The lasing spectrum recorded with the OSA reveals lasing at 1560 nm. Spectral width of the laser line is narrower than the resolution of our OSA (0.1 nm) and could not be resolved. From the linear relation between the pump and the laser output, the threshold pump power is estimated as 12 μW [160].

4.3. Temporal laser operations

Research on Er^{3+}-doped fiber lasers revealed that laser operation under continuous pump condition can be CW or self-pulsing (SP) depending on the concentration of Er^{3+} ions in the host matrix [161, 162]. Here SP operation refers to spontaneous self-pulsation in which the lasing signal appears as an infinite pulse train. It was demonstrated in fiber lasers that, for low (high) Er^{3+} concentrations, the laser output intensity was CW (SP) for any pumping rate. For concentrations in between, the output intensity varied from SP to CW when increasing the pump power. We observed and reported similar behaviors in Er^{3+}-doped microtoroidal lasers [160, 163]. With input pump powers less than 2 mW, the microlaser operates in CW regime (Fig. 14a) for Er^{3+} concentrations below 7×10^{18} cm^{-3} and in SP regime

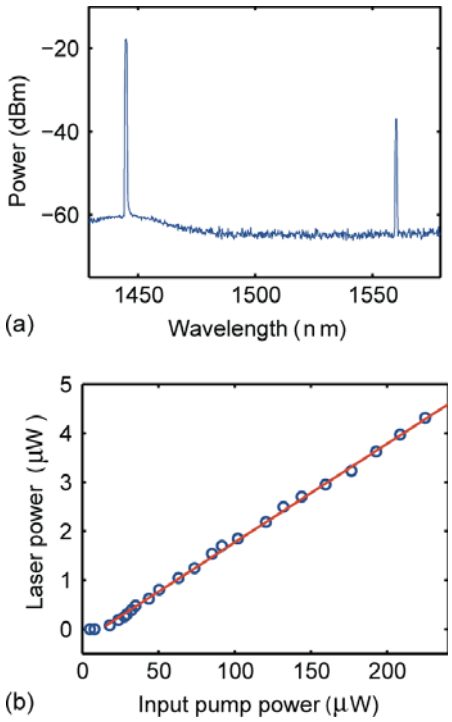

Figure 13 (online color at: www.lpr-journal.org) Lasing characterization. (a) Lasing spectrum showing pump at 1445 nm and lasing at 1560 nm. (b) Measurement of the laser output versus input pump power.

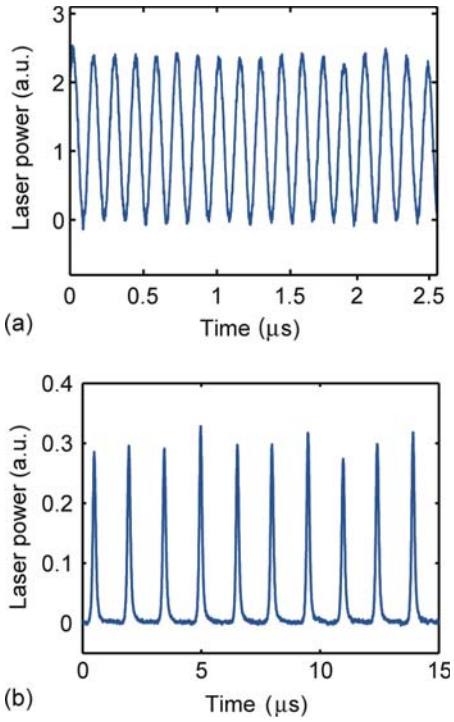

Figure 14 (online color at: www.lpr-journal.org) Laser emission in time domain from Er^{3+}-doped microtoroids. (a) CW operation measured from a microlaser with Er^{3+} concentration $\sim 5 \times 10^{18}$ cm^{-3}. The modulation of the laser power at frequency 6.7 MHz is attributed to the splitting of the laser mode. (b) SP operation with pulse width ~ 130 ns and pulse repetition rate 680 kHz measured from a microtoroid laser with Er^{3+} concentration of 2×10^{19} cm^{-3}.

(Fig. 14b) for Er^{3+} concentrations above 10^{19} cm^{-3}. In between, both CW and SP laser operations can be obtained by adjusting the intracavity pump power, e. g., varying the input pump power, adjusting the taper-resonator coupling, or exciting the pump modes of different Q factors.

Interestingly, in Fig. 14a, the laser power shows a sinusoidal oscillation at frequency 6.7 MHz. Such oscillation is not observed for the unabsorbed pump light. We have demonstrated that the oscillations are due to the intracavity Rayleigh back-scattering induced frequency splitting in the microlaser cavity [163, 164]. This can be intuitively explained as follows. Eigenmodes of a circular resonator are two-fold degenerate traveling wave modes (TWMs) propagating in opposite directions with identical polarization and resonant frequency. Coupling of the counter-propagating modes via back-scattering or reflection can lift the degeneracy leading to two standing wave modes (SWMs) whose resonant frequencies are spectrally separated from each other, i. e., frequency splitting [165–168]. In a microlaser, the lasing frequency corresponding to a cavity mode splits into two. The two lasing frequencies are photomixed in a PD with a bandwidth larger than the frequency splitting, leading to a beat note signal. The frequency of this beat note corresponds to the amount of the frequency splitting. This explains the oscillation of the laser power output in Fig. 14a. In the Er^{3+}-doped microtoroid, frequency splitting may be induced by ion clusters or inhomogeneities of the cavity structure, both of which act as the scattering centers.

Figure 14b depicts the SP laser operation from a microlaser with Er^{3+} concentration of 2×10^{19} cm^{-3}. Generation of the pulse train is attributed to the ion-ion interactions [161, 162, 169, 170]. As ion concentration increases, average distance between the ions decreases. This enhances the ion-ion interactions and leads to so called ion pairs, in which cooperative energy transfer between ions occurs. For example, when two adjacent ions are excited to state $^4I_{13/2}$, one transfers its energy to the other one and decays to the ground state $^4I_{15/2}$ non-radiatively, while the other ion is upconverted to $^4I_{9/2}$ where it mostly relaxes to $^4I_{13/2}$ non-radiatively. The net effect is the loss of one excited ion, i. e., loss of one potential stimulated photon. In other words, the paired ions inside the resonator act as saturable absorbers or as an additional loss mechanism, giving rise to self-pulsation. We observed that in the presence of frequency splitting, CW laser intensity was modulated by a beat note signal as shown in Fig. 14a. However, in Fig. 14b we did not see similar oscillation in the pulse train because the period of the beat note is longer than the pulse width. For a larger frequency splitting, when the beat note period is smaller than the pulse width, the effect of splitting shows up, as seen in Fig. 15.

For Er^{3+} concentrations in the range of 7×10^{18}–10^{19} cm^{-3}, both CW and SP lasing operations were observed

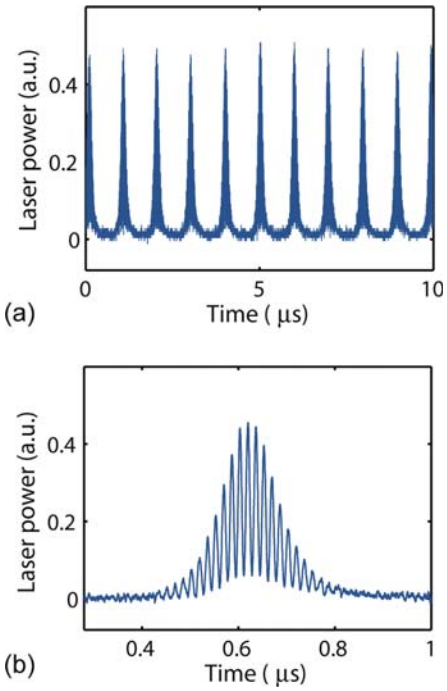

Figure 15 (online color at: www.lpr-journal.org) SP lasing operation in the presence of frequency splitting in a laser cavity. The plot in (b) is a close-up of (a) for a single pulse. The pulse is modulated by a frequency of 62 MHz.

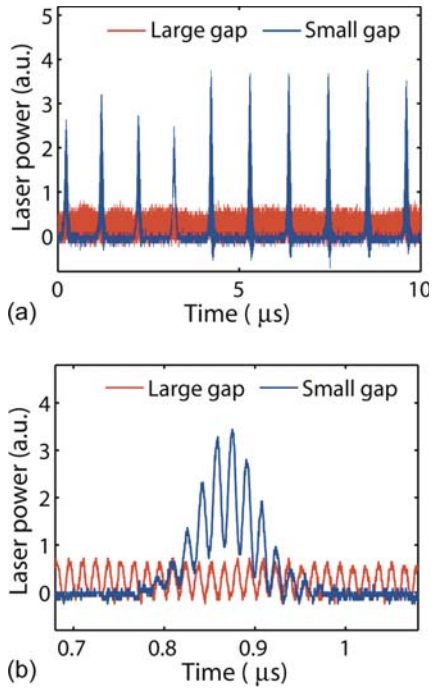

Figure 16 (online color at: www.lpr-journal.org) Laser power output at different taper-cavity coupling conditions with the same input pump power. The concentration of Er^{3+} ions is 10^{19} cm^{-3}. (a) For a large taper-cavity gap (under-coupling regime), CW operation is obtained (red curves). When reducing the gap to deep over-coupling regime, SP laser emission occurs (blue curves). (b) Close-up of the laser emission in (a).

by controlling the coupling condition, the pump power, and the Q factor of the pump mode. For example, we observed in experiments that, in the same microlaser, when the pump wavelength was tuned on resonance with a low Q cavity mode, SP operation occurred, whereas CW operation took place when the pump was on resonance with a high Q cavity mode. This is because the pumping rate in the resonator system depends on the intracavity pump power which is a function of the Q factor of the pump mode, the input pump power, and the taper-cavity coupling. They, in return, can be used to control the laser operations. Figure 16 shows the laser operation changing from CW to SP when the distance between the taper and the cavity is reduced.

4.4. Self-pulsing laser emission

Here, we discuss in detail the formation of SP operations in heavily Er^{3+}-doped microtoroidal lasers and investigate the dependence of the pulse repetition time and pulse width on the pump power and the taper-cavity coupling condition.

In heavily doped cavities, clusters of Er^{3+} ions cause a large excited state absorption due to energy transfer among paired ions which is responsible for the SP laser operation [160, 169, 170]. In the pumping process, as more ions are excited to the higher energy level, energy transfer between paired ions increases, leading to an increase in the total loss of the cavity system (i. e., cavity loss and excited state absorption loss). As a result, a large population inversion is built up and more energy is stored in the gain medium. As soon as the gain exceeds the total loss, lasing starts and laser intensity rapidly builds up in the cavity because of the large amount of energy stored in the gain medium. Subsequently, the number of ions in the excited state decreases. This decreases the total loss of the cavity due to the reduced excited state absorption. As the pump continuously replenishes the population inversion, lasing output keeps increasing as shown in the rising side of the pulse until the saturation of the gain. Subsequently, lasing output reaches its peak and starts to decrease, which slows down the reduction of ions in the excited state and consequently increases the chances of excited state absorption. As a result, the lasing output decreases further as the excited state absorption loss increases. The reduction of laser intensity continues until the lasing photons are consumed. With the pump continuously exciting the system, another cycle starts. This process repeats to generate an infinite laser pulse train. The property of the pulse depends on the pumping rate in the cavity which affects the population inversion and the laser oscillation process.

Figure 17 shows the effect of input pump power on the pulse repetition time (T), pulse width ($\Delta\tau$, full-width at half maximum), and pulse repetition rate when the taper-cavity coupling is fixed [160]. Both T and $\Delta\tau$ decrease with increasing pump. This can be explained as follows. At a higher pump power, the recovery of population inversion is achieved faster due to the higher pumping rate. Thus the

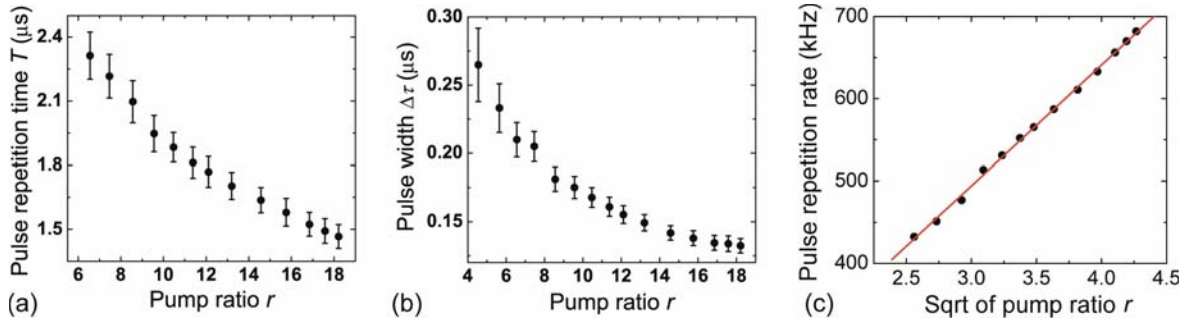

Figure 17 (online color at: www.lpr-journal.org) Study of SP laser operation in a microtoroid laser. Dependence of pulse repetition time (a) and pulse width (b) on input pump power. Pump ratio r denotes the input pump power normalized by the threshold pump power. Data points and error bars represent the mean and standard deviation of multiple measurements. (c) Pulse repetition rate versus square root of the pump ratio. Red line shows a linear fitting. (Reprinted with permission from [160])

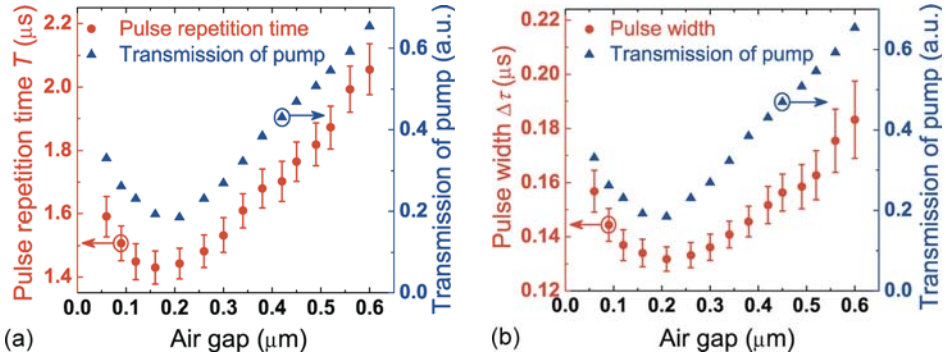

Figure 18 (online color at: www.lpr-journal.org) Dependence of pulse repetition time (a) and pulse width (b) on the taper-cavity gap. Blue triangles are the cavity loading curve for the pump mode, i. e., pump transmission versus gap. Red dots represent the pulse repetition time (a) and pulse width (b). Data points and error bars denote the mean and standard deviation of multiple measurements. The arrows direct the data points to the corresponding y axis. (Reprinted with permission from [160])

time interval between the end of a pulse and the start of the consecutive pulse, which is the time needed to create population inversion for lasing, is shorter. During the pulse generation, a higher pumping rate leads to a faster growth of net gain and thus a faster buildup of the pulse. The measured laser pulse in our experiments is almost symmetric, indicating that the fall time is close to the rise time. This is because similar mechanisms, such as coupling condition, pumping rate and cavity loss, affect both the growth and decay rate of the net gain, which determine the rise time and fall time of the pulse. Therefore, for a fixed taper-cavity coupling, increasing pump power leads to decrease in the pulse period and pulse width. It is shown in Fig. 17c that the pulse repetition rate increases linearly with the square root of the pumping level.

Figure 18 shows the effect of taper-cavity coupling on the pulse train [160]. As the gap increases, coupling between the fiber taper and the cavity decreases. At the critical coupling point of the pump light (i. e., minimum pump transmission), the intracavity pump power achieves its maximum, leading to minimized pulse repetition time and pulse width. In the under-coupling regime, as gap decreases, both T and $\Delta\tau$ decrease monotonously until the critical coupling point. Further decrease of the gap to the over-coupling regime leads to increasing T and $\Delta\tau$. In Fig. 18b, $\Delta\tau$ is longer in the over-coupling regime than that in the under-coupling regime for identical pump transmission. This is because in the over-coupling regime, laser photons generated from stimulated emission are extracted from the cavity at a higher rate due to the stronger taper-cavity coupling. This leads to a slower buildup rate of the laser pulse within the cavity and thus a longer $\Delta\tau$.

4.5. Maximum laser power output

Laser power coupling out of a microlaser cavity is determined by the output coupling coefficient and the circulating laser power within the cavity [171]. In our experiments, the same fiber taper is used to couple light in and out of the microlaser. Thus, the coupling condition which is optimized for the pump light may not be the optimal condition for extracting the laser light from the cavity and vice versa. In general, the coupling condition will affect (i) the pump-cavity coupling efficiency and hence the intracavity pump power, and (ii) the coupling loss experienced by the lasing mode which in turn determines the lasing threshold and the extraction rate of laser power from the cavity. Therefore,

the maximum laser power output does not necessarily coincide with the critical coupling point of the pump light. The optimum laser output and the corresponding coupling condition depend on the taper size, the field distributions of the pump and the laser modes, and the intrinsic cavity loss. The situation should be considered case-by-case for each individual microlaser [172]. Our measurement results in Fig. 19 show the pump transmission and the laser power output as a function of the taper-cavity coupling strength for CW and SP operations. In these measurements, the maximum laser power output occurs in the over-coupling regime of the pump light.

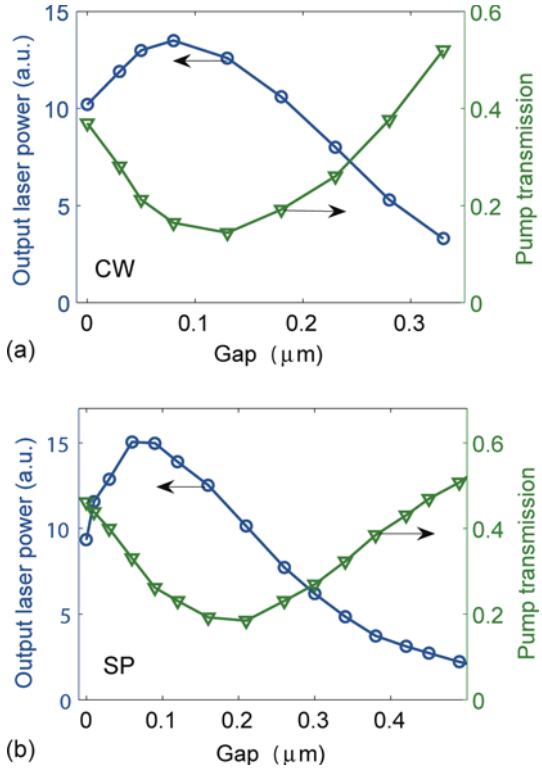

Figure 19 (online color at: www.lpr-journal.org) Laser power output versus taper-cavity gap for CW (a) and SP (b) laser operations. The circles denote the laser power output, and the triangles represent the normalized transmission of the pump light. The arrows direct the data points to the corresponding y axis. The laser power in (b) is the peak power of the pulses.

4.6. Lasing threshold

Laser threshold is achieved when the small-signal gain generated from the excited active medium equals the total loss of the resonator system. Below the threshold, optical gain increases linearly with the intracavity pumping power which depends on the input pump power, cavity Q factor, and taper-cavity coupling strength. The value of the gain is also closely related to the size of the resonator and the dopant concentration. In the following discussion, the dependence of the threshold input pump power on those parameters is considered.

4.6.1. Cavity Q factor

In the microlaser cavity, pumping rate R_{pump} is proportional to the ratio of the intracavity pump power P_c to the mode area A, i. e., $R_{\text{pump}} \propto P_c/A$. From Eq. (2), it is seen that for a fixed input power P_{in}, the intracavity power P_c is proportional to the Q factor. A higher cavity Q factor results in a longer photon lifetime in the resonator and hence more light energy stored in the cavity. Therefore, the higher the cavity Q, the higher the pumping rate and thus the lower the lasing threshold [172].

4.6.2. Taper-cavity coupling

The taper-cavity coupling strength has a two-fold effect on the lasing threshold, since it affects both the pump and laser modes. On one hand, the coupling strength affects the intracavity pump power (i. e., in Eq. (1), η is directly related to κ_{ex}) and thus the pumping rate. On the other hand, the coupling strength has impact on the total loss experienced by the laser mode. The threshold increases in the over-coupling regime due to the increased coupling loss, and in the under-coupling regime due to inefficient pump coupling from the fiber taper to the cavity [53, 172]. This is demonstrated in Fig. 20 which shows the lasing threshold as a function of the taper-cavity gap measured for an Er^{3+}-doped microtoroid [53].

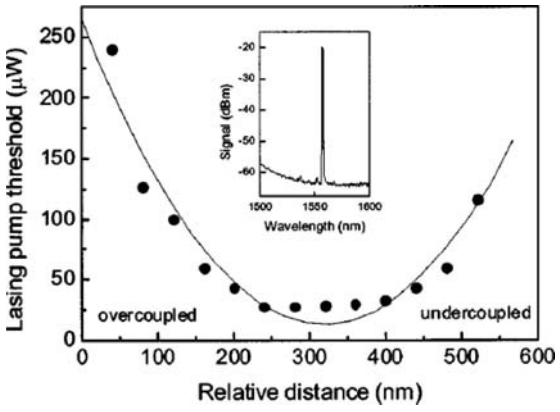

Figure 20 Lasing threshold as a function of the relative distance between a fiber taper and an Er^{3+}-implanted microtoroid. The inset shows a single-mode lasing spectrum measured under 1465 nm pumping. (Reprinted with permission from [53]. Copyright 2004, American Institute of Physics.)

4.6.3. Cavity size

The pumping rate is inversely proportional to the mode area. An efficient way to decrease the mode area is to work with resonators of smaller sizes. As the cavity size shrinks, the mode is more confined within the resonator giving rise to a smaller mode area [9, 50, 173]. This leads to an increased intracavity light intensity and thus a reduced threshold pump power. As shown in Fig. 21, the mode area decreases as the

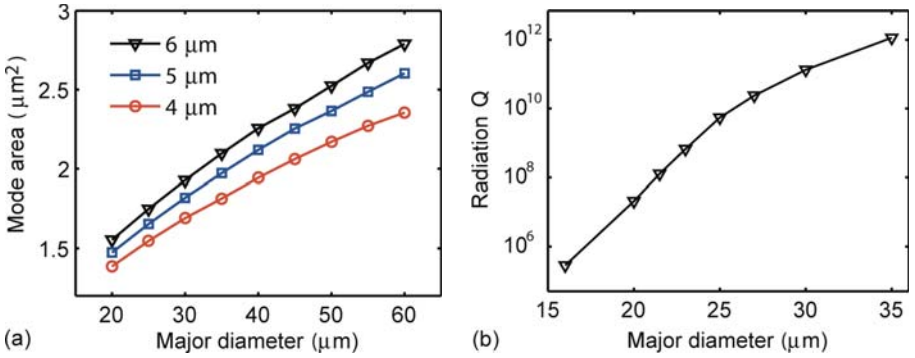

Figure 21 (online color at: www.lpr-journal.org) Simulation results of a microtoroidal resonator showing the mode area (a) and the radiation loss-induced Q factor (b) versus major diameters of microtoroids with minor diameters of 6, 5, and 4 μm.

microtoroid major and minor diameters decrease. When the diameter of a microtoroid is larger than 22 μm, ultra-high cavity Q ($> 10^8$) can be maintained as shown Fig. 21b; below 22 μm, the Q factor decreases substantially due to the increased radiation loss. This puts a practical limit on the size of microlasers. To shrink the cavity size as well as the mode volume, one can fabricate the laser cavity with host materials of larger refractive index [88, 89], integrate a photonic crystal (PC) structure with the cavity to use the PC forbidden band for light confinement [174], or introduce metallic coating on the cavity to support surface mode at the metal-dielectric interface [175–179]. Plasmonic effect at the metal-dielectric interface can be used to overcome optical diffraction limit and confine electromagnetic fields in much smaller volumes than pure dielectric materials.

4.6.4. Er^{3+} concentration

The concentration of Er^{3+} ions directly influences the optical gain obtained in the laser cavity and thus affects the lasing threshold. For a fixed cavity Q, there exists a minimum Er^{3+} concentration to produce enough gain to compensate for the round trip loss experienced by photons to achieve laser oscillation. The minimum concentration to obtain lasing increases with decreasing cavity Q [172].

For a laser cavity with a given Q factor, there exists an optimal Er^{3+} concentration which gives the lowest threshold input pump power. In lower concentration limit, a higher pump power is needed to excite Er^{3+} ions in order to provide sufficient gain overcoming the total loss. This leads to a higher threshold power. For higher ion concentrations, excited state absorption and cooperative upconversion take place, quenching the excited ions and reducing the level of population inversion. The quenching effect lowers the fraction of excited ions, and thus reduces the pumping efficiency and increases the lasing threshold. Figure 22 shows the effect of Er^{3+} concentration on the threshold pump power for silica microtoroids [172].

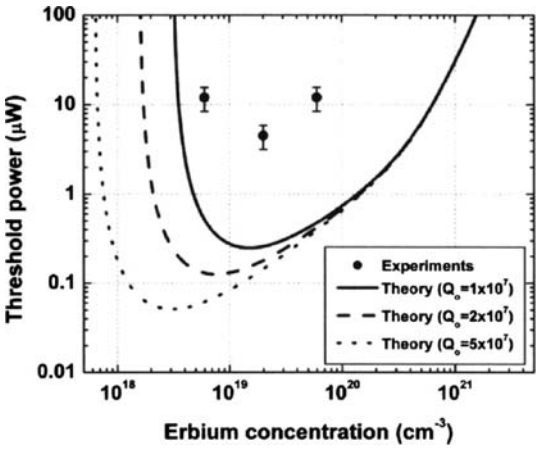

Figure 22 Minimum threshold pump power as a function of Er^{3+} concentration in microtoroids with major diameter of 50 μm for three different intrinsic Q factors. (Reprinted with permission from [172])

4.7. Upconversion

Upconversion lasing in rare-earth doped materials occurs when active ions are excited to higher energy levels through either multi-photon absorption or energy transfer between excited ions. Upconversion process produces laser emission at a wavelength significantly shorter than the pump wavelength. Using different rare-earth ions, upconversion lasing with a wide wavelength range from ultraviolet to infrared has been demonstrated [180–183]. The energy levels of different rare-earth ions can be found in [183, 184].

For Er^{3+} ions pumped in 980 nm or 1480 nm band, green light emission due to upconversion is the most common observation, which is the result of direct transition of excited ions from $^4S_{3/2}$ and $^2H_{11/2}$ levels to ground state $^4I_{15/2}$. The simplified energy level diagrams and pumping schemes are shown in Fig. 23 [185, 186]. Different mechanisms are responsible for pumping the ions to higher energy levels. Their contribution varies at different Er^{3+} concentrations [187].

The first demonstration of room-temperature CW upconversion lasing in an Er^{3+}-doped fluorozirconate fiber was reported in [181]. Laser dynamics at 540 nm and 1550 nm was studied in [185]. Upconversion efficiency of rare-earth ions is related to the intermediate level lifetime of the ions which depends on the phonon frequency of the host material and the concentration of active ions [188]. Host matrix with low phonon energy will reduce the non-radiative loss induced by multiphonon relaxation and thus realize strong upconversion. With increasing Er^{3+} concentration, photon absorption enhances, resulting in stronger upconversion emission.

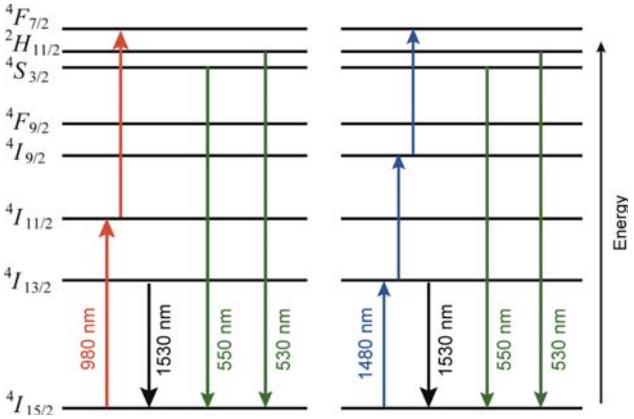

Figure 23 (online color at: www.lpr-journal.org) Energy level diagrams of Er^{3+} in silica glass and the associated electron transition processes for generating green upconversion emission under excitation at 980 nm and 1480 nm.

However, at a very high doping level, interactions between ions take place and increase the non-radiative loss which reduces the upconversion efficiency.

Green emission has been reported in different host materials with low phonon energy, such as LiLuF4 [189] and ZBLAN (ZrF_4-BaF_2-LaF_3-AlF_3-NaF) [190, 191]. Green upconversion lasing from Er^{3+} -doped ZBNA (ZrF_4-BaF_2-NaF-AlF_3) microspheres was reported with the threshold power as low as 3 µW [192]. In Er^{3+}-doped silica glass, lifetime of state $^4S_{3/2}$ is around 0.7 µs which is much shorter than that in ZBLAN. However, by increasing the Q factor of the WGM resonator, low-threshold green upconversion laser is possible. In [193], green lasers were demonstrated in Er^{3+}-doped silica microtoroids with lasing threshold of 690 µW when pumping at 1458 nm. We have observed upconversion emission from Er^{3+}-microtoroids as shown in Fig. 24. Green light emission is clearly seen along the periphery of the microtoroid.

5. Directional coupling of laser emission

The WGM microresonators provide good cavities for low-threshold lasing. However, due to the rotational symmetry of the resonator structure, the evanescent wave exists at every reflecting point. This leads to a uniform laser output in all directions and therefore inefficient power output coupling. To overcome these drawbacks and achieve directional light emission, structural symmetry of the resonator should be broken either by a waveguide for light coupling or by forming the so-called asymmetric or deformed resonators [194, 195].

The first demonstration of directional emission from a deformed microdisk laser was reported in 1993 [196]. A linear grating around the circumference of a semiconductor microdisk was produced by electron-beam lithography. The patterned asymmetries provided control of direction and intensity of light output without dramatically increasing the laser threshold. Afterwards, deformed resonators such as stadium-shaped microdisks [197, 198], spiral-shaped microcavities [99, 129, 199–201], triangle-shaped resonators [202, 203], limaçon-shaped cavities [204–206], peanut-shaped resonators [207, 208], and deformed microspheres [209, 210] have been reported to achieve directional or even unidirectional lasing with enhanced laser power output. Coupled cavities were demonstrated for unidirectional light emission with high Q modes maintained [211–213]. The coupled cavity system usually consists of a circular cavity that provides high Q WGMs and a deformed cavity which plays the role as a coupler to guide laser light out of the cavity system for directional emission.

Another alternative approach towards directional emission is to introduce defects, e. g., scatterer or notch, on the microlaser to break the symmetry [214–216]. Due to the small defect size, the cavity Q factor is still high to maintain the low lasing threshold. At the same time, directional coupling increases the laser output coupling efficiency. Figure 25 presents the SEM images of several asymmetric microcavity lasers.

6. Sensing applications

Microlasers are of great interest as ultra-sensitive sensors due to their narrow linewidths capable of reporting slight changes in resonance that would not be resolved by passive resonators [59, 163]. In this section, we focus on the label-free sensing applications employing microlasers.

Passive WGM resonators have been extensively investigated for their potential impact on chemical and bio-sensing. Their high Q factors and small mode volumes lead to strong light-matter interactions which help achieve ultra-sensitive and label-free detection. The basic principle is to track the spectral changes of a resonant mode in response to changes

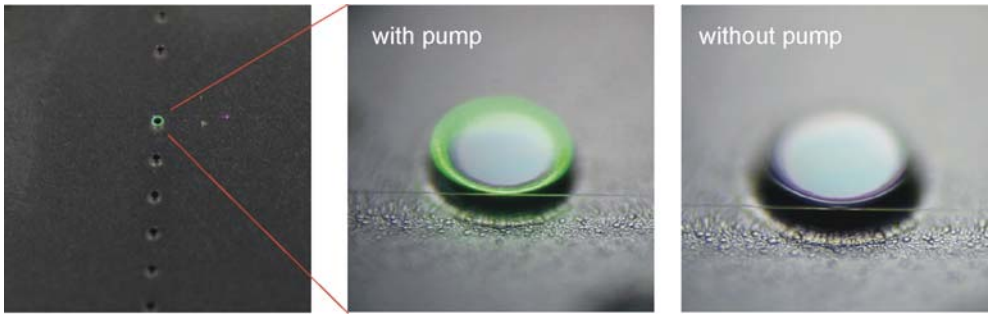

Figure 24 (online color at: www.lpr-journal.org) Green upconversion from an Er^{3+}-doped silica microtoroid with Er^{3+} concentration of 2×10^{19} cm^{-3}. The diameter of the microtoroid is around 100 µm.

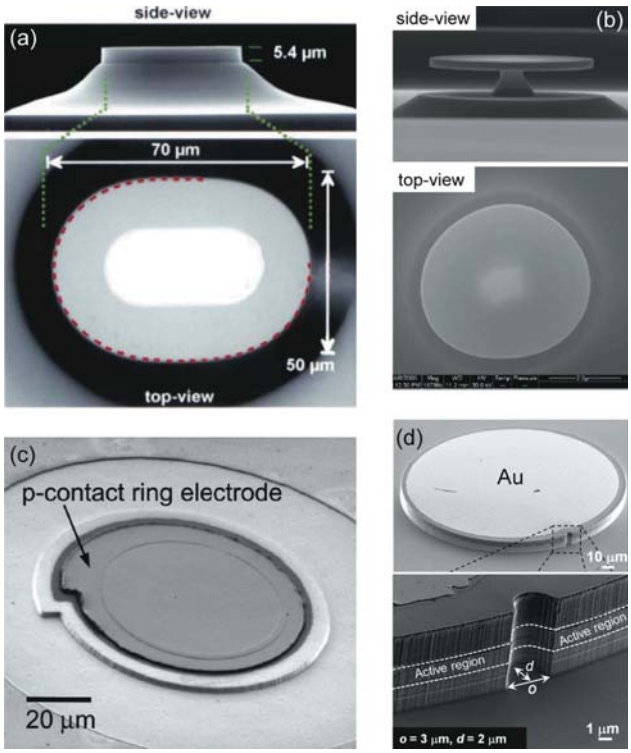

Figure 25 (online color at: www.lpr-journal.org) Asymmetric microcavity lasers. (a) SEM images of side and top view of a flattened quadrupolar-shaped cylinder laser. (Reprinted with permission from [197]) (b) SEM images of side and top view of a GaAs microdisk on top of $Al_{0.68}Ga_{0.32}As$ pedestal. (Reprinted with permission from [205]) (c) SEM image of a spiral-shaped microdisk laser diode with a disk radius of 50 μm. The p-contact ring electrode defines the areas through which carriers are injected into the microdisk and where stimulated emission can take place. (Reprinted with permission from [200]. Copyright 2004, American Institute of Physics.) (d) SEM image of a notched-elliptical resonator (upper) and zoom-in view of the device showing the smooth sidewall of the laser cavity (lower). (Reprinted with permission from [216])

in the environment near the resonator surface, e. g., refractive index shift due to changes in the surrounding, or binding of nanoscale targets such as biomolecules, viruses, or nanoparticles onto the resonator surface [217–226]. As a result of those changes, the resonant cavity mode will experience spectral shift [220, 221] and/or splitting [222–224] which can be tracked for sensing. Illustration in Fig. 26 shows the two detection mechanisms for the measurement of nanoscale objects. A tunable laser is generally used to obtain the spectral properties of the resonant mode of interest by repeatedly scanning the wavelength across the mode.

The resonance shift in a passive resonator is easily perturbed by fluctuations in the frequency of the tunable laser and by environmental noises (e. g., temperature, humidity). Such interfering perturbations will reduce the sensing resolution. However, they are minimized in the mode splitting based detection scheme. Since, in general, the split modes are affected in a similar way by the external common noises, the splitting between them, i. e., relative frequency separation, remains unperturbed [227]. Changes in the mode splitting carry the information of particles and can be used to measure those particles. Mode splitting in a microtoroidal resonator has been used to detect and size single nanoparticles and viruses by measuring the frequency and linewidth differences between the split modes [222, 228].

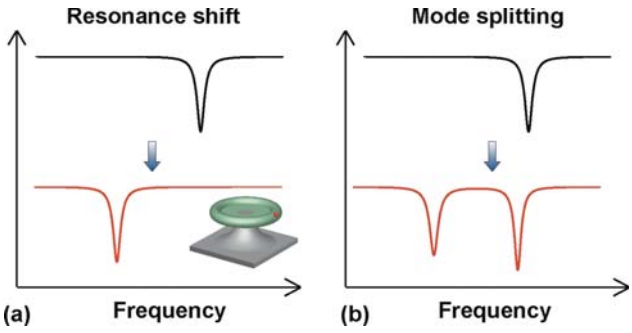

Figure 26 (online color at: www.lpr-journal.org) Sensing mechanisms using WGM resonators: resonance shift (a) and mode splitting (b) in response to nanoparticles falling into the cavity mode volume. Inset in (a) is an illustration showing a particle attached on a microtoroid surface.

The ultimate detection resolution for passive resonator based sensing schemes is limited by the resonator Q factor which determines the spectral linewidth. In a microcavity laser, the laser operation narrows down the linewidth due to stimulated emission. As a result, Q factor of the lasing mode is much higher than that of the passive cavity. Therefore, sensing resolution is greatly enhanced if a microcavity laser is used as the sensing element [59]. Sensing with microlasers has been demonstrated in previous work [229–231]. In [229], ultraviolet microdisk lasers were used to sense organic compounds. The adsorption of chemical molecules to the disk surface shifts the lasing frequency. Simulation results in [230] show that linewidth of a microsphere laser is 10^4-fold narrower than the linewidth of the corresponding passive cavity, and thus is suggested to detect low concentrations of chemicals or biomolecules. In [231], Nile red doped polystyrene microspheres were used to study the adsorption kinetics of bovine serum albumin (BSA), showing an eightfold improvement of the signal-to-noise ratio and a threefold increase in the Q factor when operated above threshold.

For cold-cavity Q of 10^8, the laser linewidth can be as narrow as a few Hertz [142, 232], allowing ultra-sensitive detection. One major challenge of the sensing is to trace such narrow laser lines. Heterodyne detection is usually employed for this purpose [142, 233]. We have demonstrated that for nanoparticle detection, mode splitting based sensing using a microlaser greatly simplified the detection scheme while still keeping the high detection resolution [59]. When a WGM microlaser is used as the sensing element, scatterer-induced split laser frequencies are photomixed in a photodetector resulting in a beat note signal, as explained in Sect. 4.3. The beat note signal corresponds to the frequency splitting and can be tracked to detect the targets. This self-heterodyne detection scheme simplifies the measurement of changes in the laser frequency. Figure 27 shows the real-time

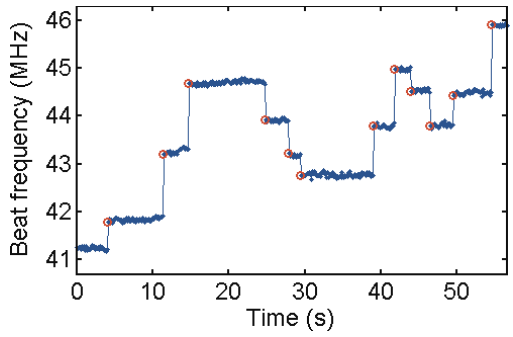

Figure 27 (online color at: www.lpr-journal.org) Real-time beat frequency as gold particles of radius 25 nm are continuously deposited onto the surface of an Er^{3+}-doped microtoroidal laser. Red circles indicate the particle binding events.

beat frequency as gold nanoparticles are continuously deposited onto a microlaser surface. Discrete jumps in the beat frequency are clearly seen above the noise level. Each individual jump indicates one particle binding event [59, 163]. Using mode splitting in a microlaser, we have successfully detected gold nanoparticles as small as 10 nm in radius and polystyrene nanoparticles of 15 nm. Detection of single virus was also demonstrated indicating its feasibility for bio-sensing. The minimum detectable particle size was limited by fluctuations of the beat frequency, which was much larger than the spectral width of the laser line itself and could be reduced by conducting the measurements in a more controlled environment [221].

7. Conclusions and outlook

This review introduced a variety of microlasers using microscale WGM cavities fabricated with different materials, such as liquid droplet, glass, semiconductor, crystalline, and polymer. By choosing the cavity structure and gain material, lasing wavelength from ultraviolet to infrared has been demonstrated. The performance of laser emission, in terms of temporal operation, maximum laser power output, and lasing threshold, was studied in Er^{3+}-doped microtoroidal lasers. In general, high Q factors, small cavity sizes, and proper dopant concentrations are responsible for low-threshold and narrow-linewidth lasing.

In addition to serving as light sources, microlasers have been used for high-performance label-free sensing. In this scheme, the laser source itself acts as the sensing device, greatly simplifying the sensor configuration. Moreover, the ultra-narrow spectral width of the laser line allows higher detection sensitivity than passive cavities, opening a new direction in highly sensitive biochemical detection. Localized plasmon effect in WGM cavities can further improve the detection resolution by local enhancement of light field which will enhance the interaction between the sensing field and the environment. This has been demonstrated in passive resonators [234–236]. Shopova et al. observed that by functionalizing a microsphere surface with metal nanoparticles (e. g., gold, silver), resonance shift induced by a single particle binding at the plasmonic hot spot was significantly enhanced [234]. Such effect can be applied to microlasers. The developments of WGM-plasmon hybrid resonators pave the way for label-free detection at the single molecule and protein level.

For dense on-chip integration, there is an increasing interest toward nanoscale lasers as light sources. For many years it has been thought that laser size is ultimately limited by optical diffraction which limits the cavity size around the order of light wavelength. Recently, it has been reported that such limit could be overcome by plasmonic effects. With the help of surface-plasmons at the metal-dielectric interface, the optical energy can be confined in a very small dimension, making cavity sizes below light wavelength within reach. In previous work, some encouraging results have been reported [175, 176, 237]. More work needs to be done regarding the high optical losses of plasmonic materials.

Another challenging issue for microlasers could be the implementation of broad-band pumping. This will avoid the need for resonantly matched laser sources to pump laser cavities, and may have an immediate and considerable impact on solar-pumped lasers. Cascaded energy transfer among different gain media has been demonstrated providing efficient broad-band pumping [57]. Gain materials with broad absorption bands and large absorption coefficients are desired for broad-band excitation.

Acknowledgements. We gratefully acknowledge the support from NSF under Grant No. 0907467 and No. 0954941.

Received: 12 July 2011, **Revised:** 8 January 2012,
Accepted: 17 January 2012

Published online: 28 February 2012

Key words: Laser, microcavity, microlaser, WGM, resonator, sensing.

Lina He received the B. S. and M. S. degrees in electronic engineering from Tsinghua University, Beijing, China, in 2005 and 2007, respectively. She is currently working toward the Ph. D. degree in electrical and systems engineering at Washington University in St. Louis, MO. Her current research interests are mainly in the areas of whispering gallery mode microcavities and related applications in lasing and sensing.

Şahin Kaya Özdemir received the B. S. and M. S. degrees in electrical and electronics engineering from the Middle East Technical University, Ankara, Turkey, in 1992 and 1995, respectively, and the Ph. D. degree in electronics engineering from Shizuoka University, Hamamatsu, Japan, in 2000. During 2000–2003 he was with the Japan Science and Technology Agency (JST), Core Research for

Evolutional Science and Technology (CREST) Research Team at The Graduate University for Advanced Studies (Sokendai), Hayama, Japan, and then served as a specially appointed foreign professor at Sokendai during 2003–2004. During 2004–2008 and 2008–2009, he was, respectively, with the JST Solution-Oriented Research for Science and Technology (SORST) program as a project group leader and with the JST Exploratory Research for Advanced Technology (ERATO) program as a researcher both at Osaka University, Osaka, Japan. Since January 2009, he is with the Dept. of Electrical and Systems Engineering, Washington University in St. Louis, MO as a research associate. He has authored or co-authored more than 70 peer-reviewed papers in various fields ranging from optical microcavities, quantum optics and quantum information processing to optical feedback interferometry and SPR sensors.

Lan Yang is an assistant professor in the Department of Electrical and Systems Engineering at Washington University in St. Louis. She received the M. S. degree in Materials Science and Ph. D. degree in Applied Physics in 2000 and 2005, respectively, from Caltech. Her current research interests include novel photonic materials and ultra-high quality optical resonators for lasing, sensing and nonlinear optics. She has more than 50 refereed technical publications and received NSF CAREER Award in 2010 for her work on real-time particle detection using an on-chip optical resonator. She is also a recipient of the Presidential Early Career Award for Scientists and Engineers (PECASE) in 2011.

References

[1] T. H. Maiman, Nature **187**, 493–494 (1960).
[2] H. J. Kimble, Phys. Scr. **T76**, 127–137 (1998).
[3] M. Pelton, J. Vukovic, G. S. Sholomon, A. Scherer, and Y. Yamamoto, IEEE J. Quantum Electron. **38**, 170–177 (2002).
[4] Ş. K. Özdemir, J. Zhu, L. He, and L. Yang, Phys. Rev. A **83**, 033817 (2011).
[5] V. Bulović, V. G. Kozlov, V. B. Khalfin, and S. R. Forrest, Science **23**, 553–555 (1998).
[6] V. V. Vassiliev, V. L. Velichansky, V. S. Ilchenko, M. L. Gorodetsky, L. Hollberg, and A. V. Yarovitsky, Opt. Commun. **158**, 305–312 (1998).
[7] C. Spiegelberg, J. Geng, Y. Hu, Y. Kaneda, S. Jiang, and N. Peyghambarian, J. Lightwave Technol. **22**, 57–62 (2004).
[8] C. G. B. Garrett, W. Kaiser, and W. L. Bond, Phys. Rev. **124**, 1807–1809 (1961).
[9] V. B. Braginsky, M. L. Gorodetsky, and V. S. Ilchenko, Phys. Lett. A **137**, 393–397 (1989).
[10] M. L. Gorodetsky, A. A. Savchenkov, and V. S. Ilchenko, Opt. Lett. **21**, 453–455 (1996).
[11] K. J. Vahala, Nature **424**, 839–846 (2003).
[12] A. B. Matsko and V. S. Ilchenko, IEEE J. Sel. Top. Quantum Electron. **12**, 3–14 (2006).
[13] V. S. Ilchenko and A. B. Matsko, J. Sel. Top. Quantum Electron. **12**, 15–32 (2006).
[14] A. Chiasera, Y. Dumeige, P. Féron, M. Ferrari, Y. Jestin, G. N. Conti, S. Pelli, S. Soria, and G. C. Righini, Laser Photon. Rev. **4**, 457–482 (2010).
[15] J. Ward and O. Benson, Laser Photon. Rev. **5**, 553–570 (2011).
[16] M. L. Gorodetsky and V. S. Ilchenko, Opt. Commun. **113**, 133–143 (1994).
[17] M. K. Chin and S. T. Ho, J. Lightwave Technol. **16**, 1433–1446 (1998).
[18] A. Serpenguzel, S. Arnold, and G. Griffel, Opt. Lett. **20**, 654–656 (1995).
[19] J. C. Knight, N. Dubreuil, V. Sandoghdar, J. Hare, V. Lefevre-Seguin, J. M. Raimond, and S. Haroche, Opt. Lett. **20**,1515–1517 (1995).
[20] V. S. Ilchenko, X. S. Yao, and L. Maleki, Opt. Lett. **24**, 723–725 (1999).
[21] J. C. Knight, G. Cheung, F. Jacques, and T. A. Birks, Opt. Lett. **22**, 1129–1131 (1997).
[22] M. Cai, O. Painter, and K. J. Vahala, Phys. Rev. Lett. **85**, 74–77 (2000).
[23] S. M. Spillane, T. J. Kippenberg, O. J. Painter, and K. J. Vahala, Phys. Rev. Lett. **91**, 043902 (2003).
[24] A. Ashkin and J. M. Dziedzic, Phys. Rev. Lett. **38**, 1351–1354 (1977).
[25] H. B. Lin and A. J. Campillo, Phys. Rev. Lett. **73**, 2440–2443 (1994).
[26] S. Uetake, R. S. D. Sihombing, and K. Hakuta, Opt. Lett. **27**, 421–423 (2002).
[27] H. M. Tzeng, K. F. Wall, M. B. Long, and R. K. Chang, Opt. Lett. **9**, 499–501 (1984).
[28] S. X. Qian, J. B. Snow, H. M. Tzeng, and R. K. Chang, Science **231**, 486–488 (1986).
[29] H.-B. Lin, J. D. Eversole, and A. J. Campillo, J. Opt. Soc. Am. B **9**, 43–50 (1992).
[30] J. Schäfer, J. P. Mondia, R. Sharma, Z. H. Lu, A. S. Susha, A. L. Rogach, and L. J. Wang, Nano Lett. **8**, 1709–1712 (2008).
[31] M. Humar and I. Muš,evi, č, Opt. Express **19**, 19836–19844 (2011).
[32] A. Kiraz, A. Kurt, M. A. Dündar, and A. L. Demirel, Appl. Phys. Lett. **89**, 081118 (2006).
[33] A. Kiraz, A. Sennaroglu, and S. Doganay, M. A. Dündar, A. Kurt, H. Kalaycioglu, and A. L. Demirel, Opt. Commun. **276**, 145–148 (2007).
[34] S.-Y. Teh, R. Lin, L.-H. Hung, and A. P. Lee, Lab Chip **8**, 198–220 (2008).
[35] M. Tanyeri, R. Perron, and I. M. Kennedy, Opt. Lett. **32**, 2529–2531 (2007).
[36] S. K. Y. Tang, Z. Li, A. R. Abate, J. J. Agresti, D. A. Weitz, D. Psaltis, and G. M. Whitesides, Lab Chip **9**, 2767–2771 (2009).
[37] W. Lee, Y. Sun, H. Li, K. Reddy, M. Sumetsky, and X. Fan, Appl. Phys. Lett. **99**, 091102 (2011).
[38] V. Sandoghdar, F. Treussart, J. Hare, V. LefevreSeguin, J. M. Raimond, and S. Haroche, Phys. Rev. A **54**, R1777-R1780 (1996).
[39] M. Cai, O. Painter, K. J. Vahala, and P. C. Sercel, Opt. Lett. **25**, 1430–1432 (2000).
[40] F. Lissillour, D. Messager, G. Stephan, and P. Feron, Opt. Lett. **26**, 1051–1053 (2001).
[41] L. Yang and K. J. Vahala, Opt. Lett. **28**, 592–594 (2003).
[42] H. Takashima, H. Fujiwara, S. Takeuchi, K. Sasaki, and M. Takahashi, Appl. Phys. Lett. **90**, 101103 (2007).

[43] C. H. Dong, Y. F. Xiao, Z. F. Han, G. C. Guo, X. S. Jiang, L. M. Tong, C. Gu, and H. Ming, IEEE Photon. Technol. Lett. **20**, 342–344 (2008).
[44] G. Lin, O. Tillement, Y. Candela, M. Martini, and Z. Cai, V. Lefévre-Seguin, and J. Hare, Proc. SPIE **7716**, 771622 (2010).
[45] S. I. Shopova, G. Farca, A. T. Rosenberger, W. M. S. Wickramanayake, and N. A. Kotov, Appl. Phys. Lett. **85**, 6101–6103 (2004).
[46] P. T. Snee, Y. Chan, D. G. Nocera, and M. G. Bawendi, Adv. Mater. **17**, 1131–1136 (2005).
[47] J. Kalkman, A. Polman, T. J. Kippenberg, K. J. Vahala, and M. L. Brongersma, Nucl. Instrum. Methods B **242**, 182–185 (2006).
[48] R. Roy, Science **238**, 1664–1669 (1987).
[49] D. K. Armani, T. J. Kippenberg, S. M. Spillane, and K. J. Vahala, Nature **421**, 925–928 (2003).
[50] S. M. Spillane, T. J. Kippenberg, K. J. Vahala, K. W. Goh, E. Wilcut, and H. J. Kimble, Phys. Rev. A **71**, 013817 (2005).
[51] L. Yang, D. K. Armani, and K. J. Vahala, Appl. Phys. Lett. **83**, 825–826 (2003).
[52] L. Yang, T. Carmon, B. Min, S. M. Spillane, and K. J. Vahala, Appl. Phys. Lett. **86**, 091114 (2005).
[53] A. Polman, B. Min, J. Kalkman, T. J. Kippenberg, and K. J. Vahala, Appl. Phys. Lett. **84**, 1037–1039 (2004).
[54] E. P. Ostby, L. Yang, and K. J. Vahala, Opt. Lett. **32**, 2650–2652 (2007).
[55] H. S. Hsu, C. Cai, and A. M. Armani, Opt. Express **17**, 23265–23271 (2009).
[56] B. Min, S. Kim, K. Okamoto, L. Yang, A. Scherer, H. Atwater, and K. Vahala, Appl. Phys. Lett. **89**, 191124 (2006).
[57] C. Rotschild, M. Tomes, H. Mendoza, T. L. Andrew, T. M. Swager, T. Carmon, and M. A. Baldo, Adv. Mater. **23**, 3057–3060 (2011).
[58] E. P. Ostby and K. J. Vahala, Opt. Lett. **34**, 1153–1155 (2009).
[59] L. He, Ş. K. Özdemir, J. Zhu, W. Kim, and L. Yang, Nature Nanotechnol. **6**, 428–432 (2011).
[60] I. M. White, H. Oveys, and X. Fan, Opt. Lett. **31** 1319–1321 (2006).
[61] J. C. Knight, H. S. T. Driver, R. J. Hutcheon, and G. N. Robertson, Opt. Lett. **17**, 1280–1282 (1992).
[62] H. J. Moon, Y. T. Chough, and K. An, Phys. Rev. Lett. **85**, 3161–3164 (2000).
[63] H.-J. Moon and K. An, Appl. Phys. Lett. **80**, 3250–3252 (2002).
[64] M. Kazes, D. Y. Lewis, Y. Ebenstein, T. Mokari, and U. Banin, Adv. Mater. **14**, 317–321 (2002).
[65] H.-J. Moon, G.-W. Park, S.-B. Lee, K. An, and J.-H. Lee, Appl. Phys. Lett. **84**, 4547–4549 (2004).
[66] A. V. Malko, A. A. Mikhailovsky, M. A. Petruska, J. A. Hollingsworth, H. Htoon, M. G. Bawendi, and V. I. Klimov, Appl. Phys. Lett. **81**, 1303–1305 (2002).
[67] S. I. Shopova, H. Zhou, X. Fan, and P. Zhang, Appl. Phys. Lett. **90**, 221101 (2007).
[68] S. Lacey, I. M. White, Y. Sun, S. I. Shopova, J. M. Cupps, P. Zhang, and X. Fan, Opt. Express **15**, 15523–15530 (2007).
[69] Y. Z. Sun, S. I. Shopova, C. S. Wu, S. Arnold, and X. D. Fan, P. Natl. Acad. Sci. USA **107**, 16039–16042 (2010).
[70] X. Liu, W. Fang, Y. Huang, X. H. Wu, S. T. Ho, H. Cao, and R. P. H. Chang, Appl. Phys. Lett. **84**, 2488–2490 (2004).
[71] T. J. Kippenberg, J. Kalkman, A. Polman, and K. J. Vahala, Phys. Rev. A **74**, 051802 (2006).
[72] S. L. Mccall, A. F. J. Levi, R. E. Slusher, S. J. Pearton, and R. A. Logan, Appl. Phys. Lett. **60**, 289–291 (1992).
[73] R. E. Slusher, A. F. J. Levi, U. Mohideen, S. L. McCall, S. J. Pearton, and R. A. Logan, Appl. Phys. Lett. **63**, 1310–1312 (1993).
[74] H. Cao, J. Y. Xu, W. H. Xiang, Y. Ma, S.-H. Chang, S. T. Ho, and G. S. Solomon, Appl. Phys. Lett. **76**, 3519–3521 (2000).
[75] P. Michler, A. Kiraz, L. Zhang, C. Becher, E. Hu, and A. Imamoglu, Appl. Phys. Lett. **77**, 184–186 (2000).
[76] T. Baba and D. Sano, IEEE J. Sel. Top. Quantum Electron. **9**, 1340–1346 (2003).
[77] S. Chang, N. B. Rex, R. K. Chang, G. Chong, and L. J. Guido, Appl. Phys. Lett. **75**, 166–168 (1999).
[78] E. D. Haberer, R. Sharma, C. Meier, A. R. Stonas, S. Nakamura, S. P. DenBaars, and E. L. Hu, Appl. Phys. Lett. **85**, 5179–5181 (2004).
[79] A. C. Tamboli, E. D. Haberer, R. Sharma, K. H. Lee, S. Nakamura, and E. L. Hu, Nature Photon. **1**, 61–64 (2007).
[80] J. V. Campenhout, P. Rojo-Romeo, P. Regreny, C. Seassal, D. V. Thourhout, S. Verstuyft, L. D. Cioccio, J. M. Fedeli, C. Lagahe, and R. Baets, Opt. Express **15**, 6744–6749 (2007).
[81] M. Fujita, R. Ushigome, and T. Baba, Electron. Lett. **36**, 790–791 (2000).
[82] M. Fujita, A. Sakai, and T. Baba, IEEE J. Sel. Top. Quantum Electron. **5**, 673–681 (1999).
[83] J. P. Reithmaier, G. Sek, A. Löffler, C. Hoffman, S. Kuhn, S. Reitzenstein, L. V. Keldysh, V. D. Kulakovskii, and A. Forchel, Nature **432**, 197–200 (2004).
[84] V. N. Astratov, S. Yang, S. Lam, B. D. Jones, D. Sanvitto, D. M. Whittaker, A. M. Fox, M. S. Skolnick, A. Tahraoui, P. W. Fry, and M. Hopkinson, Appl. Phys. Lett. **91**, 071115 (2007).
[85] S. Reitzenstein, T. Heindel, C. Kistner, A. Rahimi-Iman, and C. Schneider, S. Höfling, and A. Forchel, Appl. Phys. Lett. **93**, 061104 (2008).
[86] P. Jaffrennou, J. Claudon, M. Bazin, N. S. Malik, S. Reitzenstein, L. Worschech, M. Kamp, and A. Forchel, and J.-M. Gérard, Appl. Phys. Lett. **96**, 071103 (2010).
[87] M. Fujita and T. Baba, Appl. Phys. Lett. **80**, 2051–2053 (2002).
[88] Z. Zhang, L. Yang, V. Liu, T. Hong, K. Vahala, and A. Scherer, Appl. Phys. Lett. **90**, 111119 (2007).
[89] Q. Song, H. Cao, S. T. Ho, and G. S. Solomon, Appl. Phys. Lett. **94**, 061109 (2009).
[90] R. Chen, T.-T. D. Tran, K. W. Ng, W. S. Ko, L. C. Chuang, F. G. Sedgwick, and C. Chang-Hasnain, Nature Photon. **5**,170–175 (2011).
[91] C. Gmachl, F. Capasso, D. L. Sivco, and A. Y. Cho, Rep. Prog. Phys. **64**, 1533–1601 (2001).
[92] F. Capasso, C. Gmachl, D. L. Sivco, and A. Y. Cho, Phys. Today **55**, 34–38 (2002).
[93] J. Faist, F. Capasso, D. L. Sivco, C. Sirtori, A. L. Hutchinson, and A. Y. Cho, Science **264**, 553–556 (1994).
[94] J. Faist, C. Gmachl, M. Striccoli, C. Sirtori, F. Capasso, D. L. Sivco, and A. Y. Cho, Appl. Phys. Lett. **69**, 2456–2458 (1996).
[95] C. Gmachl, J. Faist, F. Capasso, C. Sirtori, D. L. Sivco, and A. Y. Cho, IEEE J. Quantum Electron. **33**, 1567–1573 (1997).

[96] S. Gianordoli, L. Hvozdara, G. Strasser, W. Schrenk, K. Unterrainer, and E. Gornik, Appl. Phys. Lett. **75**, 1045–1047 (1999).
[97] G. Fasching, A. Benz, K. Unterrainer, R. Zobl, A. M. Andrews, T. Roch, W. Schrenk, and G. Strasser, Appl. Phys. Lett. **87**, 211112 (2005).
[98] L. A. Dunbar, R. Houdré, G. Scalari, L. Sirigu, M. Giovannini, and J. Faist, Appl. Phys. Lett. **90**, 141114 (2007).
[99] R. Audet, M. A. Belkin, J. A. Fan, B. G. Lee, K. Lin, and F. Capasso, Appl. Phys. Lett. **91**, 131106 (2007).
[100] A. A. Savchenkov, V. S. Ilchenko, A. B. Matsko, and L. Maleki, Phys. Rev. A **70**, 051804 (2004).
[101] I. S. Grudinin, A. B. Matsko, A. A. Savchenkov, D. Strekalov, V. S. Ilchenko, and L. Maleki, Opt. Commun. **265**, 33–38 (2006).
[102] V. S. Ilchenko, A. A. Savchenkov, A. B. Matsko, and L. Maleki, Phys. Rev. Lett. **92**, 043903 (2004).
[103] I. S. Grudinin and L. Maleki, Opt. Lett. **32**, 166–168 (2007).
[104] I. S. Grudinin, A. B. Matsko, and L. Maleki, Phys. Rev. Lett. **102**, 043902 (2009).
[105] J. U. Fürst, D. V. Strekalov, D. Elser, A. Aiello, U. L. Andersen, Ch. Marquardt, and G. Leuchs, Phys. Rev. Lett. **105**, 263904 (2010).
[106] T. Beckmann, H. Linnenbank, H. Steigerwald, B. Sturman, D. Haertle, K. Buse, and I. Breunig, Phys. Rev. Lett. **106**, 143903 (2011).
[107] A. A. Savchenkov, A. B. Matsko, V. S. Ilchenko, I. Solomatine, D. Seidel, and L. Maleki, Phys. Rev. Lett. **101**, 093902 (2008).
[108] J. Kippenberg, R. Holzwarth, and S. A. Diddams, Science **332**, 555–559 (2011).
[109] K. Sasagawa and M. Tsuchiya, Appl. Phys. Express **2**, 122401 (2009).
[110] J. Moore, M. Tomes, T. Carmon, and M. Jarrahi, Opt. Express **19**, 24139–24146 (2011).
[111] C. Y. Chao and L. J. Guo, J. Vac. Sci. Technol. B **20**, 2862–2866 (2002).
[112] A. L. Martin, D. K. Armani, L. Yang, and K. J. Vahala, Opt. Lett. **29**, 533–535 (2004).
[113] T. Grossmann, S. Schleede, M. Hauser, T. Beck, M. Thiel, G. v. Freymann, T. Mappes, and H. Kalt, Opt. Express **19**, 11451–11456 (2011).
[114] P. Rabiei, W. H. Steier, C. Zhang, and L. R. Dalton, J. Lightwave Technol. **20**, 1968–1975 (2002).
[115] T. Grossmann, M. Hauser, T. Beck, C. Gohn-Kreuz, M. Karl, H. Kalt, C. Vannahme, and T. Mappes, Appl. Phys. Lett. **96**, 013303 (2010).
[116] J. R. Schwesyg, T. Beckmann, A. S. Zimmermann, K. Buse, and D. Haertle, Opt. Express **17**, 2573–2578 (2009).
[117] C.-H. Dong, L. He, Y.-F. Xiao, V. R. Gaddam, Ş. K. Özdemir, Z.-F. Han, G.-C. Guo, and L. Yang, Appl. Phys. Lett. **94**, 231119 (2009).
[118] M. Kuwata-Gonokami, K. Takeda, H. Yasuda, and K. Ema, Jpn. J. Appl. Phys. **31**, L99-L101 (1992).
[119] M. Kuwata-Gonokami and K. Takeda, Opt. Mater. **9**, 12–17 (1998).
[120] M. Kuwata-Gonokami, R. H. Jordan, A. Dodabalapur, H. E. Katz, M. L. Schilling, and R. E. Slusher, Opt. Lett. **20**, 2093–2095 (1995).
[121] T. Grossmann, S. Schleede, M. Hauser, M. B. Christiansen, C. Vannahme, C. Eschenbaum, S. Klinkhammer, T. Beck, J. Fuchs, G. U. Nienhaus, U. Lemmer, A. Kristensen, T. Mappes, and H. Kalt, Appl. Phys. Lett. **97**, 063304 (2010).
[122] S. Klinkhammer, T. Grossmann, K. Lüll, M. Hauser, C. Vannahme, T. Mappes, H. Kalt, and U. Lemmer, IEEE Photon. Technol. Lett. **23**, 489–491 (2011).
[123] F. Hide, M. A. DiazGarcia, B. J. Schwartz, M. R. Andersson, Q. B. Pei, and A. J. Heeger, Science **273**, 1833–1836 (1996).
[124] N. Tessler, G. J. Denton, and R. H. Friend, Nature **382**, 695–697 (1996).
[125] M. D. McGehee and A. J. Heeger, Adv. Mater. **12**, 1655–1668 (2000).
[126] I. D. W. Samuel and G. A. Turnbull, Chem. Rev. **107**, 1272–1295 (2007).
[127] F. Hide, B. J. Schwartz, M. A. DiazGarcia, and A. J. Heeger, Chem. Phys. Lett. **256**, 424–430 (1996).
[128] A. Fujii, T. Nishimura, Y. Yoshida, K. Yoshino, and M. Ozaki, Jpn. J. Appl. Phys. **44**, L1091-L1093 (2005).
[129] A. Tulek and Z. V. Vardeny, Appl. Phys. Lett. **90**, 161106 (2007).
[130] S. V. Frolov, M. Shkunov, A. Fujii, K. Yoshino, and Z. V. Vardeny, IEEE J. Quantum Electron. **36**, 2–11 (2000).
[131] Y. Kawabe, C. Spiegelberg, A. Schülzgen, M. F. Nabor, B. Kippelen, E. A. Mash, P. M. Allemand, M. Kuwata-Gonokami, K. Takeda, and N. Peyghambarian, Appl. Phys. Lett. **72**, 141–143 (1998).
[132] S. V. Frolov, M. Shkunov, Z. V. Vardeny, and K. Yoshino, Phys. Rev. B **56**, R4363-R4366 (1997).
[133] A. Tulek, D. Akbulut, and M. Bayindir, Appl. Phys. Lett. **94**, 203302 (2009).
[134] T. Kobayashi and M. Vavasseur, J. Opt. Soc. Am. B **27**, 2014–2019 (2010).
[135] J. B. Snow, S. X. Qian, and R. K. Chang, Opt. Lett. **10**, 37–39 (1985).
[136] S. X. Qian and R. K. Chang, Phys. Rev. Lett. **56**, 926–929 (1986).
[137] A. Sennaroglu, A. Kiraz, M. A. Dündar, A. Kurt, and A. L. Demirel, Opt. Lett. **32**, 2197–2199 (2007).
[138] A. Kiraz, S. Ç. Yorulmaz, M. Yorulmaz, and A. Sennaroglu, Photonic Nanostruct. **7**, 186–189 (2009).
[139] J. Z. Zhang and R. K. Chang, J. Opt. Soc. Am. B **6**, 151–153 (1989).
[140] S. M. Spillane, T. J. Kippenberg, and K. J. Vahala, Nature **415**, 621–623 (2002).
[141] T. J. Kippenberg, S. M. Spillane, D. K. Armani, and K. J. Vahala, Opt. Lett. **29**, 1224–1226 (2004).
[142] T. Lu, L. Yang, T. Carmon, and B. Min, IEEE J. Quantum Electron. **47**, 320–326 (2011).
[143] H. Rong, A. Liu, R. Jones, O. Cohen, D. Hak, R. Nicolaescu, A. Fang, and M. Paniccia, Nature **433**, 292–294 (2005).
[144] H. S. Rong, R. Jones, A. S. Liu, O. Cohen, D. Hak, A. Fang, and M. Paniccia, Nature **433**, 725–728 (2005).
[145] H. S. Rong, S. B. Xu, Y. H. Kuo, V. Sih, O. Cohen, O. Raday, and M. Paniccia, Nature Photon. **1**, 232–237 (2007).
[146] W. P. Acker, D. H. Leach, and R. K. Chang, Opt. Lett. **14**, 402–404 (1989).
[147] T. Carmon and K. J. Vahala, Nature Phys. **3**, 430–435 (2007).
[148] J. U. Fürst, D. V. Strekalov, D. Elser, M. Lassen, U. L. Andersen, C. Marquardt, and G. Leuchs, Phys. Rev. Lett. **104**, 153901 (2010).
[149] T. J. Kippenberg, Physics **3**, 32 (2010).
[150] J. S. Levy, M. A. Foster, A. L. Gaeta, and M. Lipson, Opt. Express **19**, 11415–11421 (2011).
[151] B. Min, T. J. Kippenberg, and K. J. Vahala, Opt. Lett. **28**, 1507–1509 (2003).

[152] H. S. Rong, S. B. Xu, O. Cohen, O. Raday, M. Lee, V. Sih, and M. Paniccia, Nature Photon. **2**, 170–174 (2008).
[153] L. He, Y.-F. Xiao, C. Dong, J. Zhu, V. Gaddam, and L. Yang, Appl. Phys. Lett. **93**, 201102 (2008).
[154] T. Carmon, L. Yang, and K. Vahala, Opt. Express **12**, 4742–4750 (2004).
[155] E. Snitzer, Appl. Opt. **5**, 1487–1499 (1966).
[156] E. Snitzer and R. Woodcock, Appl. Phys. Lett. **6**, 45–46 (1965).
[157] J. Harrington, Infrared Fibers and Their Applications (SPIE Press, Bellingham, WA, 2003), p. 268.
[158] W. L. Barnes, R. I. Laming, E. J. Tarbox, and P. R. Morkel, IEEE J. Quantum Electron. **27**, 1004–1010 (1991).
[159] L. L. Hench and J. K. West, Chem. Rev. **90**, 33–72 (1990).
[160] L. He, Ş. K. Özdemir, J. Zhu, and L. Yang, Opt. Lett. **35**, 256–258 (2010).
[161] F. Sanchez, P. Leboudec, P. L. Francois, and G. Stephan, Phys. Rev. A **48**, 2220–2229 (1993).
[162] F. Sanchez and G. Stephan, Phys. Rev. E **53**, 2110–2122 (1996).
[163] L. He, Ş. K. Özdemir, J. Zhu, and L. Yang, Phys. Rev. A **82**, 053810 (2010).
[164] L. He, Ş. K. Özdemir, Y. F. Xiao, and L. Yang, IEEE J. Quantum Electron. **46**, 1626–1633 (2010).
[165] A. Mazzei, S. Gotzinger, S. Menezes Lde, G. Zumofen, O. Benson, and V. Sandoghdar, Phys. Rev. Lett. **99**, 173603 (2007).
[166] J. Zhu, Ş. K. Özdemir, L. He, and L. Yang, Opt. Express **18**, 23535–23543 (2010).
[167] S. Wang, K. Broderick, H. Smith, and Y. Yi, Appl. Phys. Lett. **97**, 051102 (2010).
[168] X. Yi, Y.-F. Xiao, Y.-C. Liu, B.-B. Li, Y.-L. Chen, Y. Li, and Q. Gong, Phys. Rev. A **83**, 023803 (2011).
[169] E. Delevaque, T. Georges, M. Monerie, P. Lamouler, and J. F. Bayon, IEEE Photon. Technol. Lett. **5**, 73–75 (1993).
[170] S. Colin, E. Contesse, P. LeBoudec, G. Stephan, and F. Sanchez, Opt. Lett. **21**, 1987–1989 (1996).
[171] A. E. Siegman, Lasers (University Science Books, Sausalito, CA, 1986), Chap. 12, p. 476.
[172] B. Min, T. J. Kippenberg, L. Yang, K. J. Vahala, J. Kalkman, and A. Polman, Phys. Rev. A **70**, 033803 (2004).
[173] K. Srinivasan, M. Borselli, O. Painter, A. Stintz, and S. Krishna, Opt. Express **14**, 1094–1105 (2006).
[174] Y.-H. Chen, Y.-K. Wu, and L. J. Guo, Appl. Phys. Lett. **98**, 131109 (2011).
[175] M. T. Hill, Y.-S. Oei, B. Smalbrugge, Y. Zhu, T. de Vries, P. J. van Veldhoven, F. W. M. van Otten, T. J. Eijkemans, J. P. Turkiewicz, H. de Waardt, E. J. Geluk, S.-H. Kwon, and Y.-H. Lee, R. Nötzel, and M. K. Smit, Nature Photon. **1**, 589–594 (2007).
[176] M. P. Nezhad, A. Simic, O. Bondarenko, B. Slutsky, A. Mizrahi, L. Feng, V. Lomakin, and Y. Fainman, Nature Photon. **4**, 395–399 (2010).
[177] M. W. Kim, Y.-H. Chen, J. Moore, Y.-K. Wu, L. J. Guo, P. Bhattacharya, and P.-C. Ku, IEEE J. Sel. Top. Quantum Electron. **15**, 1521–1528 (2009).
[178] M. W. Kim and P.-C. Ku, Appl. Phys. Lett. **98**, 201105 (2011).
[179] J. Huang, S.-H. Kim, and A. Scherer, Opt. Express **18**, 19581–19591 (2010).
[180] R. G. Smart, D. C. Hanna, A. C. Tropper, S. T. Davey, S. F. Carter, and D. Szebesta, Electron. Lett. **27**, 1307–1309 (1991).
[181] T. J. Whitley, C. A. Millar, R. Wyatt, M. C. Brierley, and D. Szebesta, Electron. Lett. **27**, 1785–1786 (1991).
[182] S. G. Grubb, K. W. Ett, R. S. Cannon, and W. F. Humer, Electron. Lett. **28**, 1243–1244 (1992).
[183] X. Zhu and N. Peyghambarian, Adv. Opt. Electron. **2010**, 501956 (2010).
[184] L. Wetenkamp, G. F. West, and H. Tobben, J. Non-Cryst. Solids **140**, 35–40 (1992).
[185] J. Y. Allain, M. Monerie, and H. Poignant, Electron. Lett. **28**, 111–113 (1992).
[186] S. Arahira, K. Watanabe, K. Shinozaki, and Y. Ogawa, Opt. Lett. **17**, 1679–1681 (1992).
[187] G. N. van den Hoven, E. Snoeks, A. Polman, C. van Dam, J. W. M. van Uffelen, and M. K. Smit, J. Appl. Phys. **79**, 1258–1266 (1996).
[188] A. Patra, C. S. Friend, R. Kapoor, and P. N. Prasad, Appl. Phys. Lett. **83**, 284–286 (2003).
[189] E. Heumann, S. Bar, K. Rademaker, G. Huber, S. Butterworth, A. Diening, and W. Seelert, Appl. Phys. Lett. **88**, 061108 (2006).
[190] W. von Klitzing, E. Jahier, R. Long, F. Lissillour, V. Lefevre-Seguin, J. Hare, J. M. Raimond, and S. Haroche, J. Opt. B, Quantum Semiclass. Opt. **2**, 204–206 (2000).
[191] Z. Meng, J. Kamebayashi, M. Higashihata, Y. Nakata, T. Okada, Y. Kubota, N. Nishimura, and T. Teshima, IEEE Photon. Technol. Lett. **14**, 609–611 (2002).
[192] Y. Wu, J. M. Ward, and S. N. Chormaic, J. Appl. Phys. **107**, 033103 (2010).
[193] T. Lu, L. Yang, R. V. A. van Loon, A. Polman, and K. J. Vahala, Opt. Lett. **34**, 482–484 (2009).
[194] T. Harayama and S. Shinohara, Laser Photon. Rev. **5**, 247 (2011);
[195] Y.-F. Xiao, C.-L. Zou, Y. Li, C.-H. Dong, Z.-F. Han, and Q. Gong, Front. Optoelectron. (China) **3**, 109–124 (2010).
[196] A. F. J. Levi, R. E. Slusher, S. L. Mccall, J. L. Glass, S. J. Pearton, and R. A. Logan, Appl. Phys. Lett. **62**, 561–563 (1993).
[197] C. Gmachl, F. Capasso, E. E. Narimanov, J. U. Nockel, A. D. Stone, J. Faist, D. L. Sivco, and A. Y. Cho, Science **280**, 1556–1564 (1998).
[198] M. Lebental, J. S. Lauret, R. Hierle, and J. Zyss, Appl. Phys. Lett. **88**, 031108 (2006).
[199] G. D. Chern, H. E. Tureci, A. Douglas Stone, R. K. Chang, M. Kneissl, and N. M. Johnson, Appl. Phys. Lett. **83**, 1710–1712 (2003).
[200] M. Kneissl, M. Teepe, N. Miyashita, N. M. Johnson, G. D. Chern, and R. K. Chang, Appl. Phys. Lett. **84**, 2485–2487 (2004).
[201] M. Hentschel and T.-Y. Kwon, Opt. Lett. **34**, 163–165 (2009).
[202] M. S. Kurdoglyan, S. Y. Lee, S. Rim, and C. M. Kim, Opt. Lett. **29**, 2758–2760 (2004).
[203] M. Hentschel, Q. J. Wang, C. Yan, F. Capasso, T. Edamura, and H. Kan, Opt. Express **18**, 16437–16442 (2010).
[204] J. Wiersig and M. Hentschel, Phys. Rev. Lett. **100**, 033901 (2008).
[205] Q. Song, W. Fang, B. Liu, S.-T. Ho, G. S. Solomon, and H. Cao, Phys. Rev. A **80**, 041807 (2009).
[206] C.-H. Yi, M.-W. Kim, and C.-M. Kim, Appl. Phys. Lett. **95**, 141107 (2009).
[207] L. Shang, L. Liu, and L. Xu, Appl. Phys. Lett. **92**, 071111 (2008).

[208] F.-J. Shu, C.-L. Zou, F.-W. Sun, and Y.-F. Xiao, Phys. Rev. A **83**, 053835 (2011).
[209] S. Chang, R. K. Chang, and A. D. Stone, and J. U. Nöckel, J. Opt. Soc. Am. B **17**, 1828–1834 (2000).
[210] Y. F. Xiao, C. H. Dong, Z. F. Han, G. C. Guo, and Y. S. Park, Opt. Lett. **32**, 644–646 (2007).
[211] X. Wu, H. Li, L. Liu, and L. Xu, Appl. Phys. Lett. **93**, 081105 (2008).
[212] J.-W. Ryu and M. Hentschel, Opt. Lett. **36**, 1116–1118 (2011).
[213] D. Y. Chu, M. K. Chin, W. G. Bi, H. Q. Hou, C. W. Tu, and S. T. Ho, Appl. Phys. Lett. **65**, 3167–3169 (1994).
[214] V. M. Apalkov and M. E. Raikh, Phys. Rev. B **70**, 195317 (2004).
[215] C. P. Dettmann, G. V. Morozov, M. Sieber, and H. Waalkens, Europhys Lett. **82**, 34002 (2008).
[216] Q. J. Wang, C. L. Yan, N. F. Yu, J. Unterhinninghofen, J. Wiersig, C. Pflugl, L. Diehl, T. Edamura, M. Yamanishi, H. Kan, and F. Capasso, Proc. Natl. Acad. Sci. USA **107**, 22407–22412 (2010).
[217] X. D. Fan, I. M. White, S. I. Shopoua, H. Y. Zhu, J. D. Suter, and Y. Z. Sun, Anal. Chim. Acta **620**, 8–26 (2008).
[218] T. Yoshie, L. Tang, and S.-Y. Su, Sensors **11**, 1972–1991 (2011).
[219] M. S. Luchansky, A. L. Washburn, M. S. McClellan, and R. C. Bailey, Lab Chip **11**, 2042–2044 (2011).
[220] F. Vollmer and S. Arnold, Nature Methods **5**, 591–596 (2008).
[221] S. I. Shopova, R. Rajmangal, Y. Nishida, and S. Arnold, Rev. Sci. Instrum. **81**, 103110 (2010).
[222] J. Zhu, Ş. K. Özdemir, Y. F. Xiao, L. Li, L. He, D. R. Chen, and L. Yang, Nature Photon. **4**, 46–49 (2010).
[223] B. Koch, L. Carson, C.-M. Guo, C.-Y. Lee, Y. Yi, J.-Y. Zhang, M. Zin, S. Znameroski, and T. Smith, Sens. Act. B, Chem. **147**, 573–580 (2010).
[224] W. Kim, Ş. K. Özdemir, J. Zhu, L. He, and L. Yang, Appl. Phys. Lett. **97**, 071111 (2010).
[225] T. Lu, H. Lee, T. Chen, S. Herchak, J.-H. Kim, S. E. Fraser, R. C. Flagan, and K. Vahala, Proc. Natl. Acad. Sci. USA **108**, 5976–5979 (2011).
[226] M. Baaske and F. Vollmer, ChemPhysChem, DOI: 10.1002/cphc.201100757
[227] L. He, Ş. K. Özdemir, J. Zhu, and L. Yang, Appl. Phys. Lett. **96**, 221101 (2010).
[228] J. Zhu, Ş. K. Özdemir, L. He, D.-R. Chen, and L. Yang, Opt. Express **19**, 16195–16206 (2011).
[229] W. Fang, D. B. Buchholz, R. C. Bailey, J. T. Hupp, R. P. H. Chang, and H. Cao, Appl. Phys. Lett. **85**, 3666–3668 (2004).
[230] J. Yang and L. J. Guo, IEEE J. Sel. Top. Quantum electron. **12**, 143–147 (2006).
[231] A. Francois and M. Himmelhaus, Appl. Phys. Lett. **94**, 031101 (2009).
[232] L. Yang, T. Lu, T. Carmon, B. Min, and K. J. Vahala, in: Proceedings of CLEO/QELS 2007, Baltimore, MD, 2007, paper CMR2.
[233] L. Richter, H. Mandelberg, M. Kruger, and P. McGrath, IEEE J. Quantum Electron. **22**, 2070–2074 (1986).
[234] S. I. Shopova, R. Rajmangal, S. Holler, and S. Arnold, Appl. Phys. Lett. **98**, 243104 (2011).
[235] J. D. Swaim, J. Knittel, and W. P. Bowen, Appl. Phys. Lett. **99**, 243109 (2011).
[236] M. A. Santiago-Cordoba, S. V. Boriskina, F. Vollmer, and M. C. Demirel, Appl. Phys. Lett. **99**, 073701 (2011).
[237] R. F. Oulton, V. J. Sorger, T. Zentgraf, R.-M. Ma, C. Gladden, L. Dai, G. Bartal, and X. Zhang, Nature **461**, 629–632 (2009).